Analyzing a turbulent pipe flow via the one-point structure tensors

Vorticity crawlers and streak shadows

Stylianou, F. S.; Pecnik, R.; Kassinos, S. C.

DOI
10.1016/j.compfluid.2016.10.010

Publication date
2016

Document Version
Final published version

Published in
Computers & Fluids

Citation (APA)
Stylianou, F. S., Pecnik, R., & Kassinos, S. C. (2016). Analyzing a turbulent pipe flow via the one-point structure tensors: Vorticity crawlers and streak shadows. *Computers & Fluids*, *140*, 450-477. https://doi.org/10.1016/j.compfluid.2016.10.010

Computers and Fluids 140 (2016) 450–477

Contents lists available at ScienceDirect

Computers and Fluids

journal homepage: www.elsevier.com/locate/compfluid

Analyzing a turbulent pipe flow via the one-point structure tensors: Vorticity crawlers and streak shadows

F.S. Stylianou[a], R. Pecnik[b], S.C. Kassinos[a,*]

[a] Computational Sciences Laboratory (UCY-CompSci), Department of Mechanical and Manufacturing Engineering, University of Cyprus, Kallipoleos Avenue 75, Nicosia 1678, Cyprus
[b] Process & Energy Department, Delft University of Technology, Leeghwaterstraat 39, 2628CB, Delft, The Netherlands

ARTICLE INFO

Article history:
Received 4 June 2016
Revised 3 October 2016
Accepted 13 October 2016
Available online 14 October 2016

Keywords:
Turbulent pipe flow
DNS
Structure tensors
Turbulence structure
Stream vector
Inactive structure
Active structure

ABSTRACT

Efforts to identify and visualize near-wall structures typically focus on the region $y^+ \gtrsim 5$, where large-scale structures with significant turbulent kinetic energy content reside, such as the high-speed and low-speed streaks associated with sweep and ejection events. While it is true that the level of the turbulent kinetic energy drops to zero as one approaches the wall, the organization of near-wall turbulence does not end at $y^+ \approx 5$. Large-scale structures with significant streamwise extent and spatial organization exist even in the immediate proximity of the wall $y^+ < 5$. These coherent structures have received less attention so far, but it would be both useful and enlightening to bring them to focus in order, on one hand, to understand them, but also to analyze their interaction with the energetic structures that reside at somewhat higher distances from the wall.

We have recently developed a rigorous mathematical and computational framework that can be used for the calculation of the turbulence structure tensors in arbitrary flow configurations. In this work, we use this new framework to compute, for the first time, the structure tensors in a fully-developed turbulent pipe flow. We perform Direct Numerical Simulation (DNS) at Reynolds number $Re_b = 5300$, based on the bulk velocity and the pipe diameter. We demonstrate the diagnostic properties of the structure tensors, by analyzing the DNS results with a focus on the near-wall structure of the turbulence. We develop a new eduction technique, based on the instantaneous values of the structure tensors, for the identification of *inactive structures* (i.e. large-scale structures without significant turbulent kinetic energy). This leads to the visualization of *"vorticity crawlers"* and *"streak shadows"*, large-scale structures with low energy content in the extreme vicinity of the wall. Furthermore, comparison with traditional eduction techniques (such as instantaneous iso-surfaces of turbulent kinetic energy) shows that the structure-based eduction method seamlessly captures the large-scale *energetic structures* further away from the wall. We then show that the one-point structure tensors reflect the morphology of the inactive structures in the extreme vicinity of the wall and that of the energy-containing large-scale structures further away from the wall. The emerging complete picture of large-scale structures helps explain the near-wall profiles of all the one-point structure tensors and is likely to have an impact in the further development of Structure-Based Models (SBMs) of turbulence.

1. Introduction

One-point measures of large-scale, energy-containing turbulence structures are important in turbulence modeling and for flow diagnostics. Kassinos and Reynolds [18] were the first to develop a comprehensive one-point mathematical formulation that can be used to quantify different aspects of the energy-containing turbulence structures. In this regard, they showed that it is possible for two turbulence fields to share the same *componentality* state, i.e. to have the same Reynolds stress tensor values R_{ij}, but yet have different underlying turbulence structure. Differences in the turbulence structure, although undetectable through the componentality information, lead to different dynamic behavior of the turbulence, for example in response to external deformation or system rotation. Hence, a complete one-point description of the turbulence requires the information contained in the structure tensors [21]. The

---

* Corresponding author.
E-mail addresses: stylianou.fotos@ucy.ac.cy (F.S. Stylianou), r.pecnik@tudelft.nl (R. Pecnik), kassinos@ucy.ac.cy (S.C. Kassinos).

http://dx.doi.org/10.1016/j.compfluid.2016.10.010

structure *dimensionality* D_{ij} gives information about the directions of independence in the turbulence, the structure *circulicity* F_{ij} gives information on the large-scale circulation in the flow, and the *inhomogeneity* C_{ij} gives the degree of inhomogeneity of the turbulence. The third-rank *stropholysis* Q^*_{ijk} becomes important when mean rotation breaks the reflectional symmetry of the turbulence [21]. Exact definitions of these tensors are given in the next section.

One-point turbulence models that use only the Reynolds stresses and the turbulence scales to characterize the turbulence are fundamentally incomplete as shown by Kassinos and Reynolds [18]. Contrariwise, Structure-Based turbulence Models (SBMs) [17,18,20,21,35,39] are a class of turbulence models that make use of the one-point turbulence tensors. SBMs hold promise for resolving inherent limitations of simple eddy-viscosity closures and of Reynolds Stress Transport (RST) models. However, an obstacle in the further development of SBMs has been the relatively scarce availability of accurate data that could be used for model calibration and validation.

The one-point structure tensors can not be extracted from experiments. Hence, one normally turns to Direct Numerical Simulations (DNS) or Large Eddy Simulations (LES) for obtaining data on the structure tensors. Even in this case, however, the specification of proper boundary conditions for the computation of the structure tensors is a daunting task. The underlying ambiguity over how one can compute the structure tensors in complex domains has discouraged the more widespread inclusion of the tensors in turbulence databases. We have only recently developed a rigorous mathematical and computational framework that can be used for the calculation of the structure tensors in arbitrary flow configurations [48]. We will refer to this as the *General Framework (GF)*. In the past, a different framework had been considered [18,21], which is only applicable in simple, wall-bounded, streamwise periodic geometries, e.g. fully-developed channel flow, pipe flow, square duct flow. We will refer to this as the *Limited Framework (LF)*. In this work, we use both aforementioned frameworks (GF and LF) to compute, for the first time, the structure tensors in fully-developed turbulent pipe flow. We perform direct numerical simulation at Reynolds number $Re_b = 5300$, based on the bulk velocity and the pipe diameter.

The main objectives of the current study are:

(a) To illustrate that LF and GF lead to different results for the structure tensors. The same was shown in a fully-developed turbulent channel flow by Vartdal [52].
(b) To explain that both LF and GF are correct, and that the aforementioned differences should be attributed to the *lack of gauge invariance* of the structure tensors.
(c) To provide arguments in favor of using the GF for the computation of the structure tensors. For example, the GF preserves the essence of the structure tensors (as defined in the homogeneous limit) even in inhomogeneous regions of the flow, whereas the LF introduces serious deviations.
(d) To provide a database for the development and validation of new or existing SBMs.
(e) To manifest the diagnostic properties of the structure tensors, by analyzing the DNS results and comparing with traditional eduction techniques (such as instantaneous iso-surfaces of Q-criterion and turbulent kinetic energy).
(f) To establish a new flow structure characterization technique that allows the identification of *inactive structures* (i.e. large-scale structures without significant turbulent kinetic energy) based on the instantaneous values of the structure tensors.

We believe that this contribution will encourage the inclusion of the structure tensors in DNS databases, thus accelerating the development of structure-based models and promoting the use of structure tensors as a flow diagnostic tool.

2. Structure tensors

2.1. Definitions

The structure tensors are determined through the fluctuating stream vector ψ'_i, defined by the equations

$$u'_i = \epsilon_{ijk}\psi'_{k,j} \qquad \psi'_{k,k} = 0 \qquad \psi'_{i,kk} = -\omega'_i\,, \tag{1}$$

where u'_i and ω'_i are the fluctuating velocity and vorticity components, and ϵ_{ijk} is the Levi-Civita alternating tensor. Hereafter, a comma followed by an index denotes partial differentiation with respect to the implied coordinate direction. The Einstein summation convention is implied on repeated Roman indices. We require ψ'_i to be divergence-free so that the simplified Poisson equation in Eq. (1) holds, a feature that is important for the physical interpretation of the resulting structure tensors as explained by Kassinos et al. [21]. To complete the stream vector definition suitable boundary conditions must be supplied [48].

Expressing the definition of the Reynolds stresses in terms of the fluctuating stream vector,

$$R_{ij} = \overline{u'_i u'_j} = \epsilon_{ipq}\epsilon_{jrs}\overline{\psi'_{q,p}\psi'_{s,r}}\,, \tag{2}$$

and using the identity

$$\epsilon_{ipq}\epsilon_{jrs} = \det\begin{pmatrix}\delta_{ij} & \delta_{ir} & \delta_{is}\\ \delta_{pj} & \delta_{pr} & \delta_{ps}\\ \delta_{qj} & \delta_{qr} & \delta_{qs}\end{pmatrix}, \tag{3}$$

leads to the constitutive relation

$$R_{ij} + D_{ij} + F_{ij} - (C_{ij} + C_{ji}) = \delta_{ij}q^2\,, \tag{4}$$

where $q^2 = R_{ii} = 2k$ is twice the turbulent kinetic energy. Based on this equation, the second-rank structure tensors are defined as

$$\text{Componentality:} \quad R_{ij} = \overline{u'_i u'_j} \qquad r_{ij} = R_{ij}/R_{kk} \tag{5a}$$

$$\text{Dimensionality:} \quad D_{ij} = \overline{\psi'_{k,i}\psi'_{k,j}} \qquad \hat{d}_{ij} = D_{ij}/D_{kk} \tag{5b}$$

$$\text{Circulicity:} \quad F_{ij} = \overline{\psi'_{i,k}\psi'_{j,k}} \qquad \hat{f}_{ij} = F_{ij}/D_{kk} \tag{5c}$$

$$\text{Inhomogeneity:} \quad C_{ij} = \overline{\psi'_{i,k}\psi'_{k,j}} \qquad \hat{c}_{ij} = C_{ij}/D_{kk}\,. \tag{5d}$$

Unlike the other structure tensors, the inhomogeneity C_{ij} is not positive semi-definite and thus the trace $C_{kk} = D_{kk} - R_{kk}$ can be negative or even zero. For this reason, C_{ij} is normalized in terms of the traces D_{kk} or F_{kk}, which by their definition are the same $D_{kk} = F_{kk}$. Another possibility would have been to normalize all structure tensors with the trace R_{kk}, but this choice is ill-defined on solid boundaries, where R_{kk} is zero. On the contrary, D_{kk} is non-zero at the walls and proves to be the most meaningful choice for normalizing all the structure tensors.

A detailed discussion on the interpretation of each structure tensor is provided by Kassinos et al. [21], but the key features are recounted here. While the structure tensors carry complementary information, the constitutive equation provides a linear dependence among them. The *componentality* R_{ij} (the Reynolds stress tensor) gives information about which components of the fluctuating velocity are more energetic. The *dimensionality* D_{ij} carries information about the directions of independence of the turbulence. To understand this, notice that the free indices in the definition of D_{ij} are associated to the gradients of ψ'_i, which tend to vanish along directions of substantial structure elongation and tend to be strongest along directions in which short structures are stacked. The *circulicity* F_{ij} identifies the directions with large-scale circulation concentrated around them. To appreciate this, notice that the free indices in the definition of F_{ij} are associated with ψ'_i, which in turn, through the Poisson equation $\psi'_{i,kk} = -\omega'_i$, represents a large-scale, smooth version of ω'_i. Finally, the *inhomogeneity* C_{ij} detects the inhomogeneity of the turbulence. In fact, the inhomogeneity tensor vanishes identically in homogeneous flows, as can be shown by recasting the inhomogeneity definition into the form

$$C_{ij} = (\overline{\psi'_i \psi'_{k,j}})_{,k} - \overline{\psi'_i \psi'_{k,kj}} . \tag{6}$$

Here, the first term is zero only in homogeneous flows, while the second term is always zero due to the specific choice $\psi'_{k,k} = 0$. The inhomogeneity is significant near solid boundaries and relaxes to zero far away from them. At intermediate distances from the wall, the magnitude C_{kk} becomes small compared to that of the other structure tensors. Since little is known on how to model C_{ij} in general flows, structure-based turbulence models, such as the Algebraic Structure-Based Model (ASBM) [3,22,27,36,42], are based on the *homogenized* tensors. These are obtained by absorbing C_{ij} inside D_{ij} and F_{ij},

$$\begin{aligned} D^{cc}_{ij} &\equiv D_{ij} - \frac{1}{2}\left(C_{ij} + C_{ji}\right) \\ F^{cc}_{ij} &\equiv F_{ij} - \frac{1}{2}\left(C_{ij} + C_{ji}\right) . \end{aligned} \tag{7}$$

Note that the homogenized tensors now satisfy $D^{cc}_{kk} = F^{cc}_{kk} = R_{kk} = q^2$.

To complete the one-point tensorial base, an additional third-rank structure tensor must be defined as one can show that it carries information that is not contained in the second-rank tensors,

$$Q_{ijk} = -\overline{u'_j \psi'_{i,k}} = \epsilon_{jrs}\overline{\psi'_{r,s}\psi'_{i,k}} . \tag{8}$$

Using the definitions of the second-rank structure tensors, one can show that

$$\epsilon_{imp}Q_{mjp} = R_{ij} \qquad Q_{ikj} - Q_{jki} = \epsilon_{ijp}R_{pk} \tag{9a}$$

$$\epsilon_{imp}Q_{pmj} = D_{ij} - C_{ij} \qquad Q_{jik} - Q_{ijk} = \epsilon_{ijp}(D_{pk} - C_{pk}) \tag{9b}$$

$$\epsilon_{imp}Q_{jpm} = F_{ij} - C_{ji} \qquad Q_{kji} - Q_{kij} = \epsilon_{ijp}(F_{pk} - C_{kp}) . \tag{9c}$$

The homogenized tensors can also be calculated from the third-rank tensor,

$$\begin{aligned} D^{cc}_{ij} &= \frac{1}{2}\left(\epsilon_{imp}Q_{pmj} + \epsilon_{jmp}Q_{pmi}\right) \\ F^{cc}_{ij} &= \frac{1}{2}\left(\epsilon_{imp}Q_{jpm} + \epsilon_{jmp}Q_{ipm}\right) . \end{aligned} \tag{10}$$

A third-rank constitutive equation connects all the structure tensors,

$$\begin{aligned} Q_{ijk} = &\frac{1}{6}\epsilon_{ijk}q^2 + \frac{1}{3}\epsilon_{ikp}R_{pj} + \frac{1}{3}\epsilon_{jip}\left(D_{pk} - C_{pk}\right) \\ &+ \frac{1}{3}\epsilon_{kjp}\left(F_{pi} - C_{ip}\right) + Q^*_{ijk} \end{aligned} \tag{11}$$

where the *Stropholysis* tensor

$$Q^*_{ijk} = \frac{1}{6}(Q_{ijk} + Q_{jik} + Q_{jki} + Q_{kji} + Q_{ikj} + Q_{kij}) \tag{12}$$

is the fully symmetric part of the third-rank structure tensor. Stropholysis literally means *"breaking by rotation"*, a mnemonic to the fact that this tensor remains zero in turbulence that has been deformed only by irrotational mean strain. However, mean and frame rotation break the reflectional symmetry of turbulence and generate Q^*_{ijk}. Once generated, the stropholysis can be further modified by irrotational mean strain [18]. It is worth noting that the bi-traces of the third-rank tensor are

$$\begin{aligned} &Q_{kik} = 0 \\ &Q_{kki} = Q_{ikk} = -\left(\overline{u'_k \psi'_i}\right)_{,k} \\ &Q^*_{kik} = Q^*_{kki} = Q^*_{ikk} = -\frac{2}{3}\left(\overline{u'_k \psi'_i}\right)_{,k} , \end{aligned} \tag{13}$$

which all vanish in homogeneous turbulence.

2.2. Non-local information

Even though the structure tensors are one-point correlations they still carry important non-local information about the structure of turbulence. We provide two arguments to support this statement.

First, the fluctuating stream vector ψ'_i (the constituent of the structure tensors) is obtained from the solution of a vector Poisson equation, namely $\psi'_{i,kk} = -\omega'_i$. The fluctuating vorticity vector field ω'_i acts as the source term for this vector Poisson equation. A basic property of the Poisson equation is that its solution at any point in the domain receives source term contributions not only from that point, but from distant points as well. Therefore, the fluctuating stream vector will contain non-local information of the flow field that is transferred to the structure tensors.

Second, the fluctuating pressure field (which contains non-local information as it emerges from a solution of a Poisson equation) is intimately connected to the structure tensors. To demonstrate this, we consider a simple problem of homogeneous turbulence subject to mean rotation. In this case, the Poisson equation for the rapid pressure fluctuations $\frac{1}{\rho}p'^r_{,kk} = -2G_{ij}u'_{j,i}$ reduces to

$$\frac{1}{\rho}p'^r_{,kk} = \overline{\omega_i}\omega'_i , \tag{14}$$

where $G_{ij} = \overline{u_{i,j}}$ is the mean deformation tensor, and $\overline{\omega_i}$ is the mean vorticity vector. In homogeneous turbulence the mean velocity gradients are uniform, and therefore if we replace the fluctuating vorticity with the Poisson equation of the fluctuating stream vector we arrive at the relation $\frac{1}{\rho}p'^r = \overline{\omega_i}\psi'_i$. Based on this expression, we can connect the Circulicity with the rapid pressure gradient

$$\frac{1}{\rho^2}\overline{p'^r_{,k}p'^r_{,k}} = \overline{\omega_i}\,\overline{\omega_j}F_{ij}. \tag{15}$$

Clearly, in this simple example F_{ij} carries the non-local information contained in the intensity of the rapid pressure gradient.

2.3. Uniquely defining the structure tensors

In our previous work [48], we have stated that the structure tensors are *gauge invariant*, which is actually misleading. The property of *gauge invariance* should be attributed only to quantities that are independent of the specific gauge conditions chosen to define uniquely the ψ'_i, i.e. the Euclid gauge condition and boundary gauge condition [40,48]. As it is shown in this work, the structure tensors do not have this property. Based on two different sets of boundary gauge conditions for ψ'_i, we have calculated two different ψ'_i fields along with their associated structure tensors. Even though both ψ'_i fields successfully reproduce the same u'_i field, they do not produce the same values for the structure tensors.

Here, we also prove analytically the lack of gauge invariance of the structure tensors. The incompressibility condition of u'_i implies the relation $u'_i = \epsilon_{ijk}\psi'_{k,j}$, which is considered as the backbone of the definition for ψ'_i. This relation does not define uniquely the ψ'_i, since adding a gradient of a scalar function θ to ψ'_i

$$\psi'_i \rightarrow \psi'_i + \theta_{,i} \tag{16}$$

still satisfies the relation between u'_i and ψ'_i. This is a consequence of the identity

$$\epsilon_{ijk}\theta_{,kj} = 0. \tag{17}$$

If we apply the *gauge transformation* Eq. (16) to the definition of the structure tensors (apart from the Reynolds stress) we can show that they are not gauge invariant. To clarify the issue of gauge invariance, we will focus on the particular example of the structure dimensionality tensor D_{ij}. If we allow for the gauge transformation of the stream vector $\psi'^{\theta}_i = \psi'_i + \theta_{,i}$, then D_{ij} transforms according to

$$D^{\psi^\theta}_{ij} \equiv \overline{\psi'^{\theta}_{k,i}\psi'^{\theta}_{k,j}} = D^{\psi}_{ij} + \overline{\psi'_{k,i}\theta_{,kj}} + \overline{\theta_{,ki}\psi'_{k,j}} + \overline{\theta_{,ki}\theta_{,kj}} \tag{18}$$

which is clearly not gauge invariant since $D^{\psi^\theta}_{ij} \neq D^{\psi}_{ij}$. Therefore, different gauge conditions (chosen to uniquely define ψ'_i) lead to different values for the structure tensors. Since the structure tensors were originally defined with the aim to describe the coherent structures of turbulence, we must identify the specific gauge conditions that preserve their intended meaning. In the following paragraphs, we provide strong arguments that point to the preferred gauge conditions.

In homogeneous flows only one gauge condition is needed to uniquely define ψ'_i. We impose the Euclid gauge condition $\psi'_{i,i} = 0$, since this particular choice imparts a number of desirable properties to the structure tensors, namely:

(a) the inhomogeneity tensor becomes identically zero in homogeneous flows (see Eq. (6)),
(b) a simple relation connects the circulicity spectrum tensor to the vorticity spectrum tensor in homogeneous flows (see [18] Section 2.6),
(c) the differential equation for the stream vector reduces to a Poisson type (see [48] Section 3.3),
(d) the relations between ψ'_i, u'_i, and ω'_i follow a recursive form: $[\psi'_{i,i} = 0,\ u'_{i,i} = 0,\ \omega'_{i,i} = 0]$, $[u'_i = \epsilon_{ijk}\psi'_{k,j},\ \omega'_i = \epsilon_{ijk}u'_{k,j}]$, $[\psi'_{i,kk} = -\epsilon_{ijk}u'_{k,j}, u'_{i,kk} = -\epsilon_{ijk}\omega'_{k,j}]$.

In inhomogeneous flows, the Euclid gauge condition alone cannot uniquely define ψ'_i. An additional boundary gauge condition must be specified. There are two possibilities:

(a) either restrict the stream vector components that are tangential to the local surface boundary: $\epsilon_{ijk}n_j\psi'_k\big|_S = \epsilon_{ijk}n_j a'_k$, which leads to the *Limited Framework (LF)*,
(b) or restrict the stream vector component that is normal to the local surface boundary: $n_i\psi'_i\big|_S = n_i a'_i$, which leads to the *General Framework (GF)*.

In both frameworks the vector surface field a'_i must satisfy specific conditions that can be found in Stylianou et al. [48], with a rigorous mathematical proof given by Quartapelle [40]. For the case of fully-developed periodic turbulent pipe flow, we can simply set $a'_i = 0$ in both formulations. As explained by Quartapelle [40], the GF is applicable in domains with any type of connectedness, while the LF is only applicable to simply connected domains. In addition to this mathematical superiority of GF, we provide below the physical arguments that point to the preference of GF over LF for the computation of the structure tensors:

(a) Through the Poisson equation $\psi'_{i,kk} = -\omega'_i$, the stream vector ψ'_i represents a large-scale, smooth version of ω'_i. The boundary gauge condition enforced on ψ'_i should preserve this property, so that the interpretation of the structure tensors remains unaffected as the wall boundary is approached. Since $n_i\omega'_i\big|_S = 0$ at the solid boundaries, the GF gauge boundary condition $n_i\psi'_i\big|_S = 0$ satisfies this requirement. This is not the case for the LF.
(b) As an inhomogeneous wall is approached, the gauge boundary condition should constrain the normal stream vector component rather than the tangential components. Constraining just the normal stream vector component is less restrictive than constraining the two tangential components. The GF does take this effect into account, but LF does not.
(c) In this work, we have calculated the structure tensors using both the GF and the LF. Comparing the results shows that the GF produces simpler profiles for the structure tensors that describe more accurately the structures of turbulence. In view of this simplicity, the modeling of structure tensors will be easier under the GF.

It should be clear that both LF and GF are correct, and that any differences in the resulting profiles of the structure tensors are attributable to their lack of gauge invariance. In light of this degree of freedom, one has to choose the gauge condition that preserves the intended meaning of the structure tensors. We comment further on this in Section 3.5.

3. Details of the present computation

DNS of fully-developed incompressible turbulent flow through a smooth pipe have been computed previously by Eggels et al. [10], Loulou et al. [29], Satake et al. [44], Wagner et al. [55], Fukagata and Kasagi [12], Veenman [53], Wu and Moin [56] and more recently by El Khoury et al. [11]. What differentiates the current work from the previous studies is the calculation of the structure tensors and their use for visualizing the near-wall structures. Computing the structure tensors involves statistical averages of the fluctuating stream vector gradient components. In the following subsections, we provide detailed information on the numerical aspects of our simulation. For validation purposes, we compare our results with the results of Eggels et al. [10], Wu and Moin [56], and El Khoury et al. [11]. Then, we proceed to present the profiles of the structure tensors along the pipe radius, and extract the physical information concerning the large-scale, energy-containing structures of turbulence. Finally, we also demonstrate how the instantaneous values of the structure tensors can be used to identify inactive structures, i.e. large-scale structures without significant energy content. Structures of this type are located adjacent to the wall.

3.1. Computational framework

For our simulations, we have used the CDP software developed at the Center for Turbulence Research (Stanford, NASA Ames). CDP is an unstructured, collocated, nodal-based, finite-volume code that solves the incompressible Navier–Stokes equations. The fractional-step method [24] is used to numerically solve the continuity and momentum equations. Briefly, an intermediate velocity is obtained from the momentum equation by using the pressure from the previous time step. A Poisson system for the pressure is solved using the intermediate velocity. The final values of the nodal and face-normal velocities are obtained by utilizing the nodal and face-normal pressure gradients to correct the corresponding intermediate values. The final velocity satisfies the incompressibility condition. The Crank–Nicolson time discretization scheme is used for the nodal velocity, present in the diffusive and non-linear terms, while the Adams-Bashforth advancement scheme is used for the face-normal velocity appearing in the non-linear term. Simple interpolation schemes are used from nodal to face quantities. Space discretization of diffusive and convective terms is treated via the Gauss theorem and the summation-by-parts (SBP) operators as explained by Ham et al. [15]. The face-centered gradient related to the diffusive/Laplacian terms are treated via a second-order accurate centered-difference scheme. A very detailed description of the numerical techniques used by this code is reported in [1,2,14,15,32,33,57].

3.2. Mesh details

Our computational resources constrained the mesh size to a maximum of approximately 5 million grid points. Taking this limitation into account, we created a computational mesh that is suitable for capturing all physical phenomena taking place in a turbulent pipe flow at low Reynolds numbers. Close to the pipe wall,

Table 1
Overview of numerical parameters, mean flow properties, and mesh resolution. Since the exact Re_τ of the simulation is not known a priori, during the construction of the mesh we have used the approximate value $Re_\tau \approx 180$ to identify the approximate viscous units.

Parameter	Eggels	Veenman	Wu and Moin	El Khoury	Stylianou
$Re_b = u_b D/\nu$	5300	5299	5300	5300	5300
$Re_\tau = u_\tau R/\nu$	180	181	181.37	181.05	181.34
u_b/u_τ	14.73	14.63	14.611	14.637	14.613
$C_f = \tau_w/(\frac{1}{2}\rho u_b^2)$	9.22×10^{-3}	9.35×10^{-3}	9.369×10^{-3}	9.336×10^{-3}	9.366×10^{-3}
$T_{\text{stats}}/(\frac{R}{u_\tau})$	8.0	20.0	20.53	~60[a]	98.54
L_x/R	10	10	15	25	15
$N_r \times N_\phi \times N_x$	3,145,728	1,785,856	67,108,864	~18,670,000	5,064,108
N_r	96	109	256	–	–
N_ϕ	128	128	512	–	–
N_x	256	128	512	–	361
Δr^+_{min}	0.94	0.11	0.17	0.14	0.333
Δr^+_{max}	1.88	4.03	1.65	~4.44	~3.500
$R\Delta\phi^+_{\text{max}}$	8.84	8.89	2.22	4.93	4.189
Δx^+	7.00	14.10	5.31	[3.03, 9.91]	7.500

[a] vailable after private communication with El Khoury et al.

viscous forces dominate and thus the mesh has to be very fine. The viscous scales

$$u_\nu = u_\tau \qquad p_\nu = \rho u_\tau^2 \qquad \delta_\nu = \frac{\nu}{u_\tau} \qquad t_\nu = \frac{\delta_\nu}{u_\tau} \tag{19}$$

for velocity, pressure, length, and time respectively, are used for normalization purposes. Normalization with the viscous scales is symbolized by superscript "+".

Our computational domain has a streamwise extent of $L_x = 15R$. The length was chosen to be the same with the one used in the study of Wu and Moin [56]. As they note in their work, experimental data suggests the existence of very large-scale motions that range in length form $8R$ to $16R$, and therefore the choice of $L_x = 15R$ is justified. The simulation was performed at bulk Reynolds number $Re_b = 5300$ by setting the following values: pipe radius $R = 1$, fluid density $\rho = 1$, bulk velocity $u_b = 1$, and kinematic viscosity $\nu = \frac{1}{5300} u_b D$ (where $D = 2R$ is the pipe diameter). In Appendix A, we explain how the specification of the previous parameters led to the averaged pressure gradient $\frac{d\overline{p_W}}{dx} = -0.009366 \frac{\rho u_b^2}{R}$ and friction velocity $u_\tau = 0.06843 u_b$. Computational details of our simulation, along with details of previous simulations by other researchers at the same Reynolds number, are summarized in Table 1.

The total number of computational grid points is 5,064,108. In the streamwise direction the number of points is $N_x = 361$, and therefore the corresponding grid resolution is $\Delta x^+ = 7.5$. In the $r - \phi$ plane, the number of points is $N_{r-\phi} = 14,028$. At the wall, the grid is structured with $N_\phi = 270$ and a grid resolution of $R\Delta\phi^+_{\text{max}} = 4.189$, $\Delta r^+_{\text{min}} = 0.333$. The structured grid extends for $N_l = 26$ layers with increasing radial ratio of $\lambda = 1.08$. Therefore, the structure mesh starts at the wall ($r = R$) and ends at a distance (measured from the axis of the pipe):

$$r = R - \Delta r_{\text{min}} \frac{\lambda^{N_l} - 1}{\lambda - 1} = 0.852. \tag{20}$$

The interior part of the pipe (unstructured part) consists of triangular prisms. In this region, the maximum radial extent of the triangles is approximately $\Delta r^+_{\text{max}} \approx 3.5$. The computational mesh in the $r - \phi$ plane (or equivalently in the $y - z$ plane) is shown in Fig. 1.

3.3. Cusp at $(R - r)^+ \approx 27$

For some line figures displayed in upcoming sections, the variables plotted with respect to the radial direction exhibit a cusp at around $(R - r)^+ \approx 27$. This is not part of the physics of the flow. It is attributed to the transition of the mesh from the regular hexahedra to the triangular prisms. A comparison of the nodal discretization and cell-centered discretization of CDP on asymmetric meshes, shows that the nodal-based formulation (the one adopted in our computations) is less sensitive to mesh asymmetries [15]. All unstructured codes are prone to this type of mesh sensitivity.

3.4. Implementational details

In order to reach the fully-developed state as fast as possible, we have set the initial velocity field to

$$u_i = \overline{u_i}^E + u_i', \tag{21}$$

where $\overline{u_i}^E$ corresponds to the DNS data of Eggels et al. [10]. Random velocity fluctuations satisfying the constrains of zero divergence and zero wall value were added, i.e. the turbulent flow was tripped with a solenoidal disturbance. One can achieve this by taking the curl of a unit random vector field ξ_i

$$u_i' = \epsilon_{ijk} \xi_{k,j} \qquad u_i'\big|_{r=R} = 0. \tag{22}$$

The time step was set to $\Delta t = 0.008 R/u_b$. This time step satisfies the viscous stability limit (VSL) and the Courant–Friedrichs–Lewy (CFL) criterion. The VSL gives

$$VSL = \nu \frac{\Delta t}{(\Delta r_{\text{min}})^2} = 0.895, \tag{23}$$

which satisfies the stability requirement. The real time CFL calculated during the simulation is given by the relation

$$CFL = \frac{\Delta t}{dV} \oint \frac{|u_i n_i| dA}{2}, \tag{24}$$

where n_i is the normal to the surface unit vector, and the surface integration dA concerns the control volume dV of each grid node. The maximum CFL fluctuates in time around $\text{CFL}_{\text{max}} \approx 0.6$, while the smallest CFL fluctuates around $\text{CFL}_{\text{min}} \approx 0.2 \times 10^{-3}$. The maximum value of the CFL is also less than one as the corresponding criterion dictates.

The initial unrealistic and uncorrelated velocity field was evolved for 30,000 time steps (equivalent to $16 \times 15R/u_b$, enough to allow a particle to travel 16 times through the pipe axial dimension at the bulk velocity), in order to ensure that the fully-developed state is reached. We also note that the entrance length needed for a pipe flow to reach the fully-developed state is given by the empirical relation $L_e \approx 1.6 R Re_b^{1/4}$, which for our Re_b number gives $27.3R$. This is many times less than the $16 \times 15R$.

The entire simulation lasted for 210,000 time steps and thus the collection of statistics took place for 180,000 time steps. This

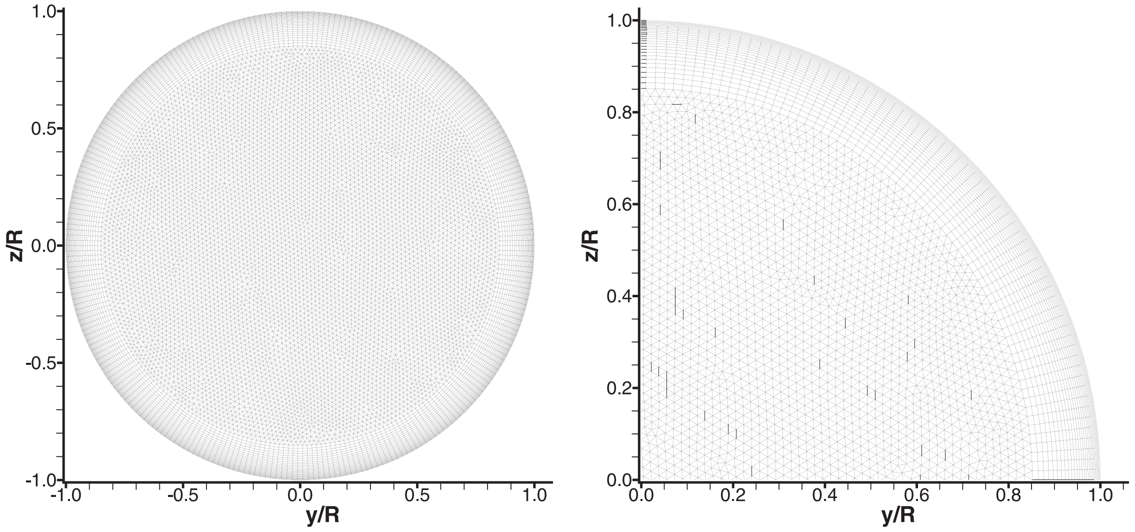

(a) (b)

Fig. 1. Computational mesh (a) in the $y-z$ plane, and (b) close up of its one quarter. Close to the wall the mesh has structured Cylindrical form, while the core of the pipe is made up of triangular prisms which form the unstructured part of the mesh.

is equivalent to $T_{\text{stats}} = 96 \times 15R/u_b$, enough to allow a fluid particle to travel 96 times through the pipe axial dimension at the bulk velocity. Expressing T_{stats} in terms of the eddy-turnover time R/u_τ we get $T_{\text{stats}} \approx 98.54R/u_\tau$, which is considerably longer than the respective times used in previous studies as indicated in Table 1. To avoid round-off errors during the time averaging process, the simulation was split into 3 equal parts of 60,000 time steps each. In each part, statistics were collected every 20 steps (i.e. 3000 samples). This approach was adopted for two reasons: (a) to avoid collecting correlated samples and (b) to avoid solving the time demanding stream vector Poisson equations at every time step. The final time averaged quantities were obtained from a simple average of the 3 aforementioned parts. In addition to averaging in time, the statistical sample was enhanced by averaging in the two homogeneous directions x and ϕ. The averaging in the streamwise direction is straightforward, while the averaging in the circumferential direction involves interpolation in a polar mesh.

3.5. Boundary conditions

The instantaneous pressure is given by the relation $p = \frac{dp_w}{dx}x + \tilde{p}$, where $\frac{dp_w}{dx}$ is the part that is explicitly set by the pressure gradient controller (see Appendix A), and $\tilde{p}$ is the part that is solved via the pressure Poisson equation in order for the incompressibility condition to be satisfied. Due to the symmetry of the flow the functional form of the mean pressure is $\overline{p}(x, r) = \frac{d\overline{p_w}}{dx}x + g(r)$ and therefore it follows that $\tilde{p} = g(r) + p'(x, r, \phi, t)$. While the mean pressure $\overline{p}$ is linear in the x direction, $\tilde{p}$ is periodic. Thus, periodic boundary conditions can be assigned to the pressure at the pipe inlet and outlet as done for the other flow variables. At the surface of the pipe wall, no-slip boundary conditions (due to impermeability and viscous forces) are applied for the velocity field (i.e. $u_i|_{r=R} = 0$), along with zero wall-normal gradient for the pressure (i.e. $\left.\frac{d\tilde{p}}{dr}\right|_{r=R} = 0$).

For the calculation of the structure tensors one needs the fluctuating stream vector, defined via the three Poisson equations of Eq. (1). These equations involve the fluctuating vorticity, which is unknown since the mean vorticity is not available a priori. To avoid this difficulty, we solve for the instantaneous stream vector, which involves the instantaneous vorticity. Due to the streamwise periodicity, the domain is considered as multiply connected and as explained by Stylianou et al. [48] and Quartapelle [40], the proper boundary conditions for the instantaneous stream vector are

$$GF: \quad \left.\frac{\partial \psi_x}{\partial r}\right|_{r=R} = 0 \quad \psi_r|_{r=R} = 0 \quad \left.\frac{\partial (r\psi_\phi)}{\partial r}\right|_{r=R} = 0. \tag{25}$$

This set of boundary conditions comprises the *General Framework (GF)* for computing the stream vector. In this framework, the wall-normal stream vector component is restricted.

Another possibility is to restrict the wall-tangential stream vector components

$$LF: \quad \psi_x|_{r=R} \overset{!}{=} 0 \quad \frac{\partial (r\psi_r)}{\partial r}|_{r=R} \overset{!}{=} 0 \quad \psi_\phi|_{r=R} \overset{!}{=} 0. \tag{26}$$

This set of boundary conditions correspond to the *Limited Framework (LF)* for computing the stream vector. The exclamation mark is used to indicate that these boundary conditions should be used with caution. As illustrated by Stylianou et al. [48], these boundary conditions create a stream vector that does not reconstruct the correct instantaneous velocity vector. There is a constant offset between the original and the reconstructed velocity. It was assumed by Vartdal [52] that this constant offset is responsible for the differences between the structure tensors calculated via GF and LF. As a matter of fact, the constant shift does not affect the values of the structure tensor components since they involve only the fluctuating part of the velocity and stream vector fields (i.e. the constant offset is canceled out). Therefore, the LF boundary conditions can be used for the calculation of the structure tensors, but not for the mean velocity field in a pipe geometry. The differences in the structure tensors generated via the GF and LF are due to the lack of gauge invariance and should in fact be expected. The choice of the GF over the LF must be based on arguments related to the physical content of the resulting tensors, as outlined in Section 2.3.

In cylindrical coordinates, both the differential equations and the boundary conditions for the stream vector components are decoupled from each other. Since our computational software is built on Cartesian coordinates we transform the boundary conditions to these coordinates. In Cartesian coordinates, the Poisson equations for the stream vector components are decoupled, while the boundary conditions are coupled. This is illustrated via the transformations

$$\psi_r = +\cos(\phi)\psi_y + \sin(\phi)\psi_z \tag{27}$$

$$\psi_\phi = -\sin(\phi)\psi_y + \cos(\phi)\psi_z , \tag{28}$$

where $\cos(\phi) = y/r$ and $\sin(\phi) = z/r$. Using a simple first-order difference scheme for the radial derivative[1], the radial and circumferential boundary conditions take the following form

$$GF\!:\begin{pmatrix}\psi_y^W\\ \psi_z^W\end{pmatrix} = \frac{-1}{1+\frac{\Delta r}{R}}\begin{pmatrix}-\sin^2(\phi) & \sin(\phi)\cos(\phi)\\ \sin(\phi)\cos(\phi) & -\cos^2(\phi)\end{pmatrix}\cdot\begin{pmatrix}\psi_y^I\\ \psi_z^I\end{pmatrix} \tag{29}$$

$$LF\!:\begin{pmatrix}\psi_y^W\\ \psi_z^W\end{pmatrix} = \frac{1}{1+\frac{\Delta r}{R}}\begin{pmatrix}\cos^2(\phi) & \sin(\phi)\cos(\phi)\\ \sin(\phi)\cos(\phi) & \sin^2(\phi)\end{pmatrix}\cdot\begin{pmatrix}\psi_y^I\\ \psi_z^I\end{pmatrix} \tag{30}$$

where W stands for the grid point on the wall, while I stands for the internal grid point in the normal direction. The simplicity of the above relation is based on the assumption that the first internal grid point away from the wall must lie along the wall-normal direction. This is the main reason that we have not used an O-grid mesh. Even though Δr is very small at the wall ($\Delta r = \delta_\nu/3 = 1.837 \times 10^{-3}$), it should never be neglected since this will reduce the ψ_ϕ boundary condition of Eq. (25) to $\left.\frac{\partial\psi_\phi}{\partial r}\right|_{r=R} = 0$, and the ψ_r boundary condition of Eq. (26) to $\left.\frac{\partial\psi_r}{\partial r}\right|_{r=R} = 0$, which are incorrect.

Initially, a sequential method was adopted to solve the stream vector equations, with inner iterations to ensure that the coupled boundary conditions are satisfied at each time step. Even though this process gives the correct solution, the convergence of the inner iterations was found to be slow. Motivated by the need of a faster convergence rate, a second coupled method was embraced. This method treats the last two components of the stream vector as fully-coupled, making the incorporation of the boundary conditions an easy task. An additional advantage of this approach is the elimination of the inner iteration process.

3.6. Validation of velocity and pressure statistics

The mean velocity profile scaled with inner and outer variables is presented in Fig. 2. Our results (denoted by “S”) are in excellent agreement with the DNS data of El Khoury et al. [11] (denoted by “K”), Wu and Moin [56] (denoted by “M”) and Eggels et al. [10] (denoted by “E”). In our simulation, the first grid point away from the wall is located at $\delta_\nu/3$, therefore the viscous sublayer is well-resolved. The data in this region follow the theoretical linear velocity distribution $\overline{u_x^+} = (R-r)^+$.

At larger distances from the wall, the “log-law” velocity distribution with “universal” constants ($\kappa = 0.41,\ B = 5.0$) is not followed. This is true even at Reynolds numbers above $Re_b = 20,000$, which is the starting point of the existence of the overlap region (where the arguments leading to “log-law” are valid) in the channel flow. Even at $Re_b = 44,000$ Wu and Moin [56] showed with their DNS data that the assumptions made by Millikan to derive the log-law are not valid. A number of studies referenced in the paper of Wu and Moin [56], rule out the applicability of a logarithmic scaling theory for Reynolds numbers at least up to $Re_b = 230,000$. Only at these very high Re_b does a separation between inner and outer scales arise. Therefore, the logarithmic trend of the data at low Re_τ (such as the present one) should not be attributed to the log-law. As explained by Wu and Moin [56] the approximate logarithmic variation of $\overline{u_x^+}$ on $(R-r)^+$ at low Re_τ is dictated by the nature of the curvature of the mean velocity gradient profile.

The mean pressure difference $\overline{p}^+(r) - \overline{p}^+(R)$ as a function of r is reported in Fig. 3. The plot compares our result to the data of El Khoury et al. [11] and Wu and Moin [56]. Eggels et al. [10] did not report the mean pressure difference. Close to the pipe wall the two results match each other, but as we move towards the pipe centerline small deviations arise. In the range $r/R = [0, 0.35]$ our results are closer to the results of El Khoury et al. [11], while in the range $r/R = [0.35, 0.75]$ our data are closer to the data of Wu and Moin [56].

The Reynolds stress components are presented in Fig. 4. Our data are in very good agreement with the data of El Khoury et al. [11] and Wu and Moin [56]. The data of Eggels et al. [10] exhibit small deviations from the data of the remaining computations, at least the normal components. The data for the shear stress component from all computations collapse at the same trend.

The pressure fluctuation statistics are reported in Fig. 5. In the near-wall region the data of El Khoury et al. [11] and Wu and Moin [56] match each other, while in the outer region small differences exist. Our data and the data of Eggels et al. [10]) in the outer region exhibit also small differences with respect to the data of Wu and Moin [56], but with reverse sign in regard to the data of El Khoury et al. [11]. The maximum value in our data is the same with the one of Wu and Moin [56], but its radial location is matches better by El Khoury et al. [11]. In the near-wall region our data exhibit the same trends with the ones of El Khoury et al. [11] and Wu and Moin [56]. The discrepancies between the four computations are attributed to the differences in the domain size, the mesh resolution, and the order of the numerical schemes applied.

4. Active and inactive structures

4.1. Terminology

In this section, we define the terms *“active structures”* and *“inactive structures”* and use them to distinguish large-scale structures with high turbulent kinetic energy content (i.e. active) from large-scale structures with low turbulent kinetic energy (i.e. inactive). These should not be confused with the already existing terminology of *“active motions”* and *“inactive motions”*. The concept of *“active motions”* and *“inactive motions”* was advanced by Townsend [49–51] and Bradshaw [6,7], in order to distinguish the motions that contribute to the wall-normal velocity fluctuations, from the motions that contribute primarily to the wall-parallel velocity fluctuations.

4.2. Identification criteria

Efforts to identify and visualize near-wall structures typically focus in the region $5 \lesssim y^+ \lesssim 50$ where large-scale structures with significant turbulent kinetic energy content reside, such as the high-speed and low-speed streaks and the associated sweep and ejection events. While it is true that the level of the turbulent kinetic energy drops to zero as ones approaches the wall, the organization of near-wall turbulence does not end at $y^+ \approx 5$. Large-scale structures with significant streamwise extent exist even in the immediate proximity to the wall and it would be both useful and enlightening to bring them to focus in order to understand them. Furthermore, it would be interesting to analyze their

---

[1] A second-order scheme for the radial derivative will not improve the overall accuracy of the method since the neighboring node distances in the streamwise and circumferential directions at the wall are one order of magnitude greater than the radial distances (see Table 1). Furthermore, the first grid points from the wall are already very close to the boundary, less than $0.5\delta_\nu$.

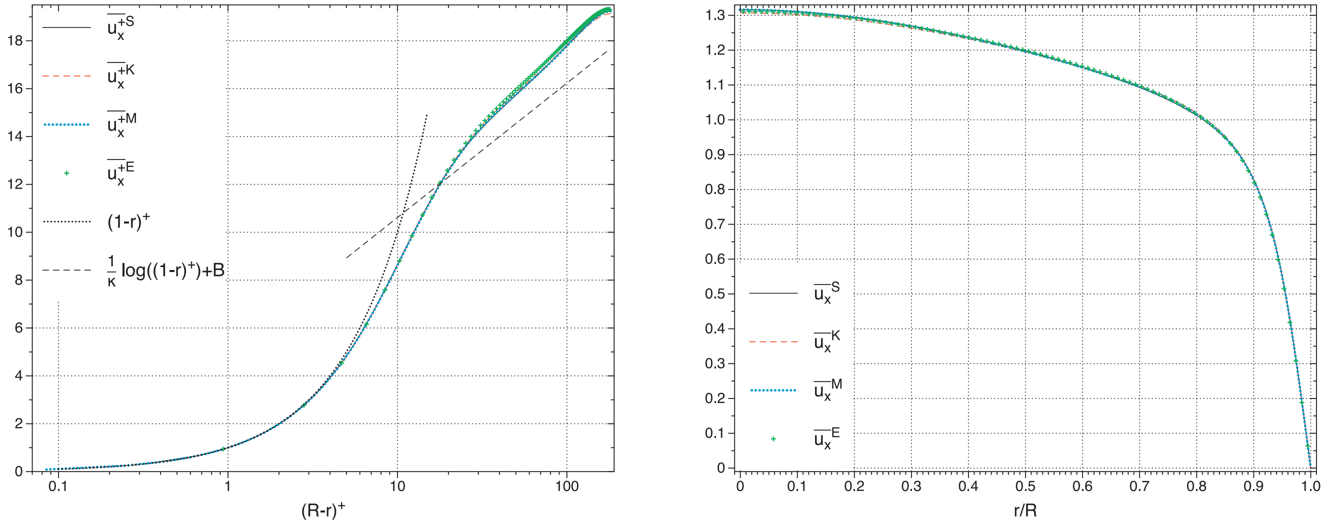

(a) (b)

Fig. 2. Mean axial velocity profile scaled with (a) wall units, and (b) bulk units.

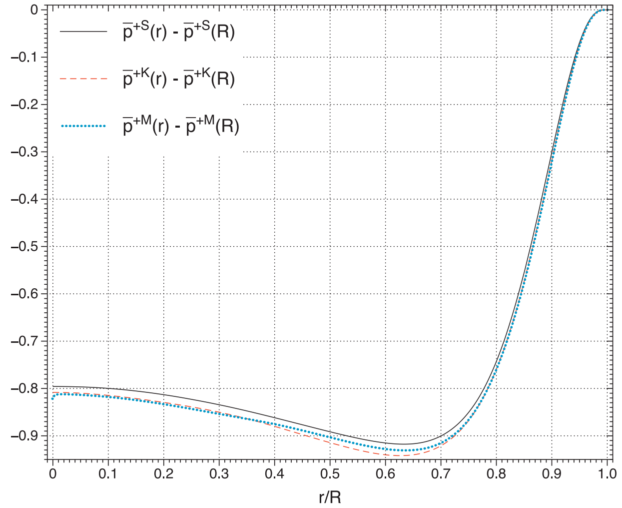

Fig. 3. Normalized mean pressure difference.

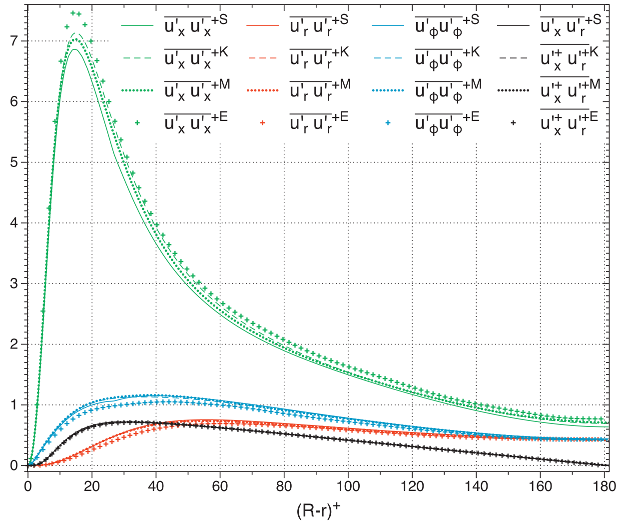

Fig. 4. Diagonal and off-diagonal Reynolds stress components normalized with wall units.

interaction with the more energetic structures that reside at somewhat higher distances from the wall. To visualize the active structures one can use iso-surfaces of high values of turbulent kinetic energy. On the other hand, a clear visualization criterion for the inactive structures does not exist. Here, we develop one such criterion.

Our treatment starts by decomposing the fluctuating stream vector gradient to a symmetric and an antisymmetric part

$$\psi'_{i,j} = \underbrace{\frac{1}{2}(\psi'_{i,j} + \psi'_{j,i})}_{S^{\psi'}_{ij}} + \underbrace{\frac{1}{2}(\psi'_{i,j} - \psi'_{j,i})}_{\Omega^{\psi'}_{ij}}. \qquad (31)$$

Recalling the stream vector definition $u'_i = \epsilon_{ijk}\psi'_{k,j}$, a direct relation between the fluctuating velocity vector u'_i and the antisymmetric tensor $\Omega^{\psi'}_{ij}$ is evident

$$u'_i = \epsilon_{ijk}\Omega^{\psi'}_{kj} \iff \Omega^{\psi'}_{kj} = \frac{1}{2}\epsilon_{kij}u'_i. \qquad (32)$$

On the other hand, the symmetric tensor $S^{\psi'}_{ij}$ does not directly contribute to the fluctuating velocity vector u'_i. In homogeneous flows with mean rotation $\overline{\omega_i}$, it can be shown that the symmetric tensor $S^{\psi'}_{ij}$ is directly related to the gradient of the rapid fluctuating pressure, $\frac{1}{\rho}p'^{r}_{,i} = S^{\psi'}_{ij}\overline{\omega_j} + \frac{1}{2}\epsilon_{ijk}\overline{\omega_j}u'_k$. Therefore, the symmetric tensor $S^{\psi'}_{ij}$ can be assumed to affect indirectly the fluctuating velocity through the gradient of the fluctuating rapid pressure that appears in the momentum transport equations. Our criterion for the identification of inactive structures involves the invariant quantity

$$Q^{\psi'} \equiv -\frac{1}{2}\psi'_{i,j}\psi'_{j,i} \qquad (33)$$

and for this reason we call it the $Q^{\psi'}$-criterion. One can rewrite the $Q^{\psi'}$ invariant in the form

$$Q^{\psi'} = \frac{1}{2}(\Omega^{\psi'}_{ij}\Omega^{\psi'}_{ij} - S^{\psi'}_{ij}S^{\psi'}_{ij}), \qquad (34)$$

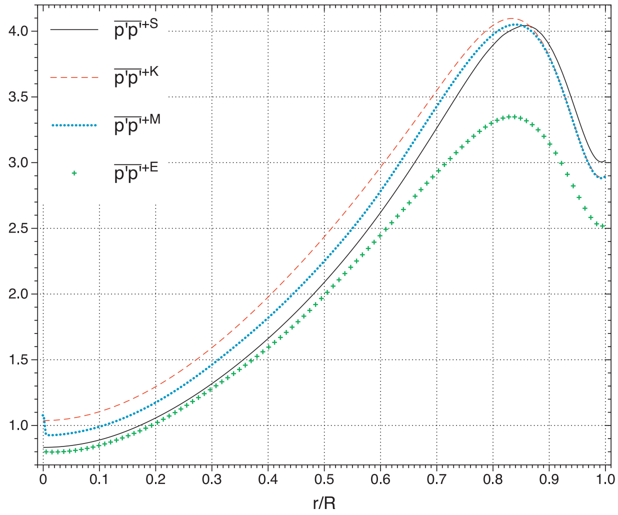

Fig. 5. Normalized pressure fluctuation statistics.

which now involves the symmetric $S_{ij}^{\psi'}$ and antisymmetric $\Omega_{ij}^{\psi'}$ tensors. Using this form, it is clear that $Q^{\psi'} < 0$ whenever the second part $S_{ij}^{\psi'} S_{ij}^{\psi'}$ is larger than the first part $\Omega_{ij}^{\psi'} \Omega_{ij}^{\psi'}$, and therefore this condition identifies large-scale structures that contribute only indirectly to the fluctuating velocity field (i.e. inactive structures).

To link all the above quantities with the definitions of the structure tensors, we note the exact relations

$$
\begin{aligned}
Q^{\psi'} &= -\frac{1}{2} C_{kk}^{t} \\
\Omega_{ij}^{\psi'} \Omega_{ij}^{\psi'} &= \frac{1}{2} R_{kk}^{t} \\
S_{ij}^{\psi'} S_{ij}^{\psi'} &= \frac{1}{2} \left(D_{kk}^{t} + C_{kk}^{t} \right) .
\end{aligned}
\tag{35}
$$

Since the above relations refer to instantaneous quantities, we have dropped the time average from the definitions of the structure tensors (hence the superscript t). Based on the above relations, it should be clear that the $Q^{\psi'} < 0$ criterion identifies regions where $C_{kk}^{t} > 0$, and hence, regions with positive values of inhomogeneity are occupied by inactive structures. According to this connection, Fig. 14 of Section 5 can be used to identify regions where the inactive structures reside on average. Based on this figure, the near-wall and centerline regions have a higher probability to host inactive structures than the region in-between the two. In the near wall region, turbulent kinetic energy drops to zero while the first invariant of dimensionality and inhomogeneity do not. This indicates that in this region we can find large-scale coherent structures that have low energy content. This is counter to the notion that large-scale structures are associated with high energy content, a link established from homogeneous arguments, where the inhomogeneity tensor is identically zero.

We have developed our stream vector based $Q^{\psi'}$-criterion along the lines that the traditional velocity-based $Q^{u'}$-criterion was developed [16]. The velocity-based criteria are built to identify coherent vortex structures [9]. Such structures are extracted from regions of $Q^{u'} > 0$, which reduces to $\Omega_{ij}^{u'} \Omega_{ij}^{u'} > S_{ij}^{u'} S_{ij}^{u'}$ and therefore to high values of the first invariant of vorticity tensor $W_{kk}^{t} > 2 S_{ij}^{u'} S_{ij}^{u'}$. Our criterion identifies regions of $\Omega_{ij}^{\psi'} \Omega_{ij}^{\psi'} < S_{ij}^{\psi'} S_{ij}^{\psi'}$ corresponding to $Q^{\psi'} < 0$. These arguments justify the use of inverted inequality conditions in the two criteria, a point that should be noted. Having this in mind, one can proceed to construct the $\lambda_2^{\psi'}$ and the $\Delta^{\psi'}$ criteria, all of which will have inverted condition symbols compared to the traditional $\lambda_2^{u'}$ and $\Delta^{u'}$ velocity criteria (for details see [9]). Any of the new stream vector based criteria ($Q^{\psi'} < 0$, $\lambda_2^{\psi'} > 0$, $\Delta^{\psi'} < 0$) could be used to identify inactive structures. However, we propose the use of $Q^{\psi'}$ since it is the only one that is expressible directly in terms of the structure tensors and thus can be more easily comprehended. For the same reason, $Q^{\psi'}$ can more easily be linked to structure-based turbulence models in order to sensitize them to the presence of near-wall inactive structures. This is a direction we plan to explore in the near future.

As we will show shortly, the condition $Q^{\psi'} > 0$ is also useful in that it can be used to identify large-scale structures with high turbulent kinetic content. In this sense, the conditions $Q^{\psi} < 0$ and $Q^{\psi} > 0$ provide a unified structure-based criterion for capturing both active and inactive structures.

4.3. Visualizations

In this subsection, we use visualization criteria to identify turbulence structures. For the identification of small-scale vortical structures we use iso-surfaces of positive values of $Q^{u'}$. For active structures we use iso-surfaces of high values of turbulent kinetic energy k^{t}. For inactive structures, we use the newly developed criterion based on the iso-surfaces of negative values of $Q^{\psi'}$. We show the inactive structures as extracted from both the LF and the GF, in order to highlight the effect of the gauge choice.

Fig. 6 represents an overview of the various types of turbulence structures appearing in a fully-developed turbulent pipe flow. The pipe domain is shown in orthogonal Cartesian and orthogonal Cylindrical coordinates. For the construction of the radial and circumferential[2] axes we use the transformations: $r = \sqrt{y^2 + z^2}$, $\phi = \text{atan2}(z, y)$. The radial and circumferential coordinates take values in the range $[0, R]$ and $(-\pi, +\pi]$ respectively. An artifact of the coordinate transformations is the stretching of the structures in the circumferential direction as we move from the wall towards the center of the pipe. The pipe wall is illustrated with gray color. High/Low-speed streaks are shown with red/blue color. Vortical structures with right/left hand sense of rotation around the positive x-axis are shown with gray/black color. Inactive structures are shown with green color. For the top/bottom part of Fig. 6 the LF/GF has been used for the computation of inactive structures. In the electronic supplementary material one can find animations of time consecutive iso-surfaces of the structures shown in Fig. 6(b) and (d).

Focusing our attention in the near region of high-speed and low-speed streaks, we see an increased vortical activity around these structures. The generation mechanism of streaks [23,26] demands the existence of vortical structures. Counter-rotating vortical structures that drive fluid towards the wall (sweep event) will generate high-speed streaks. Due to the splatting process the high-speed streaks have larger extent in the circumferential direction than in the radial direction. On the other hand, counter-rotating vortical structures that drive fluid away from the wall (ejection event) will generate low-speed streaks. Due to the bursting process the low speed streaks have smaller extent in the circumferential direction than in the radial direction.

Now we move our attention to the inactive structures. We use both the LF and the GF to compute the inactive structures. In the case of LF (Fig. 6a,b), the inactive structures reside beneath the streaks as if they are the shadow of the streaks on the wall. In the case of GF (Fig. 6c,d), the inactive structures are again adjacent to the wall, but they are located on the sides of the streaks. For the construction of the inactive structures we choose negative values of $Q^{\psi'}$. Other $Q^{\psi'}$ values closer to zero but still negative, will

---

[2] The arctangent function with two arguments atan2(_,_) is used in order to identify the appropriate quadrant of the computed angle.

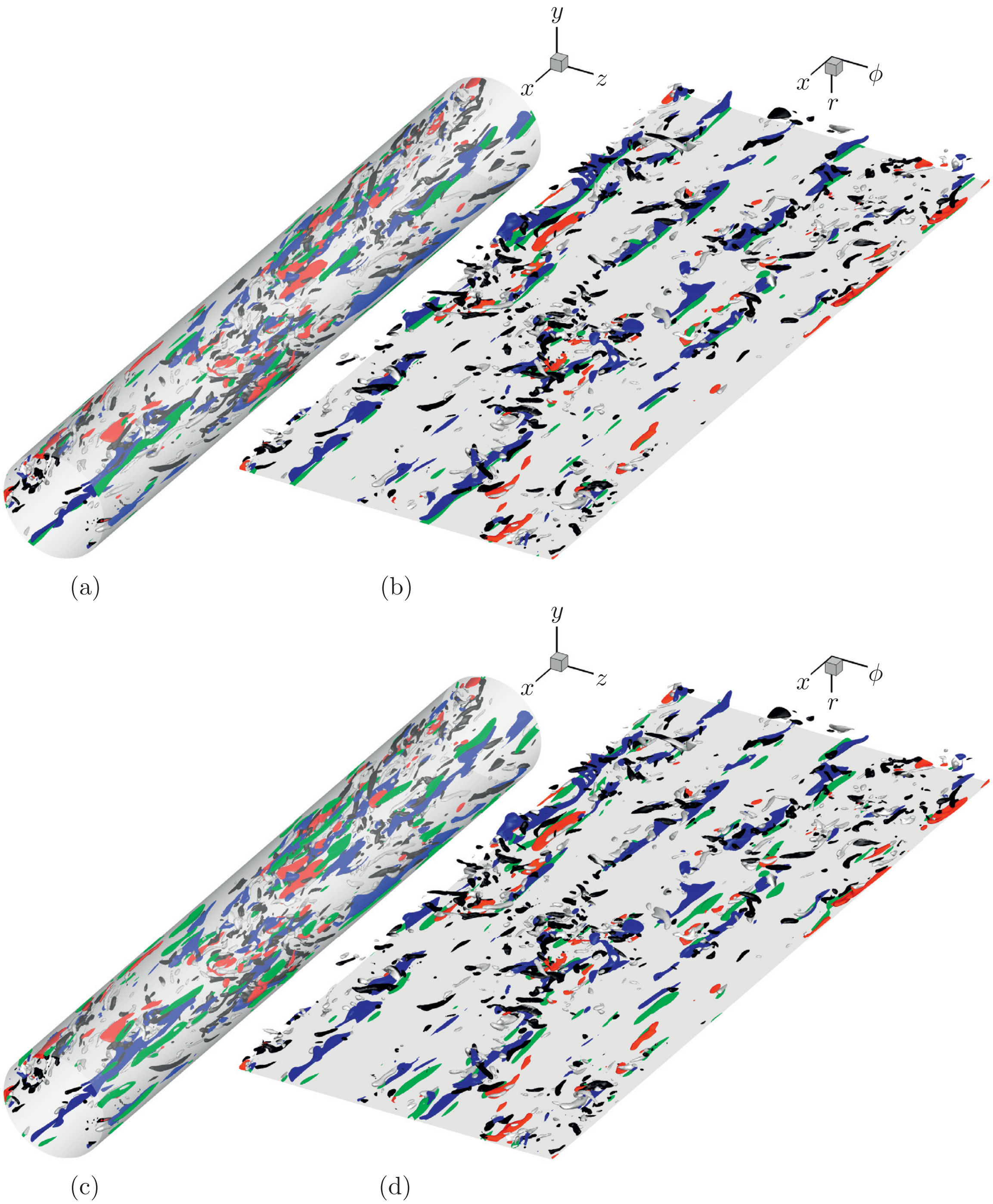

Fig. 6. Visualization of turbulence structures in (a,c) orthogonal Cartesian, and (b,d) orthogonal Cylindrical coordinate system. In (a,b)/(c,d) the LF/GF has been used for the computation of inactive structures. The pipe wall is illustrated with gray color. High/Low-speed streaks with positive/negative streamwise fluctuating velocity u'_x are shown with red/blue color. The streaks are visualized using iso-surfaces of turbulent kinetic energy with value $k^t = 3.20k^{\max}$. Vortical structures with positive/negative streamwise fluctuating vorticity ω'_x are shown with gray/black color. The vortical structures are visualized using iso-surfaces of the $Q^{u'}$-criterion with value $Q^{u'} = 0.18W_{kk}^{\max}$. Inactive structures are shown with green color. The Inactive structures are visualized using iso-surfaces of the $Q^{\psi'}$-criterion with value $Q^{\psi'} = -1.78C_{kk}^{\max}$. (For interpretation of the references to color in this figure legend, the reader is referred to the web version of this article.)

indicate regions around the active structures. Animation of the time consecutive iso-surfaces of the structures reveals that the inactive structures follow the high-speed and low-speed streaks in such a way that they are always beneath them. This is interesting since the inactive structures are located in regions with lower local velocities than the streaks. This indicates the interplay between the active and inactive structures and reveals the non-local nature of these disturbances.

Fig. 7 illustrates the radial locations where the active and inactive structures tend to exist. The active structures are generated in the region $(R-r)^+ > 5$. High-speed streaks dominate in the region $5 < (R-r)^+ < 12$ and low-speed streaks dominate in the

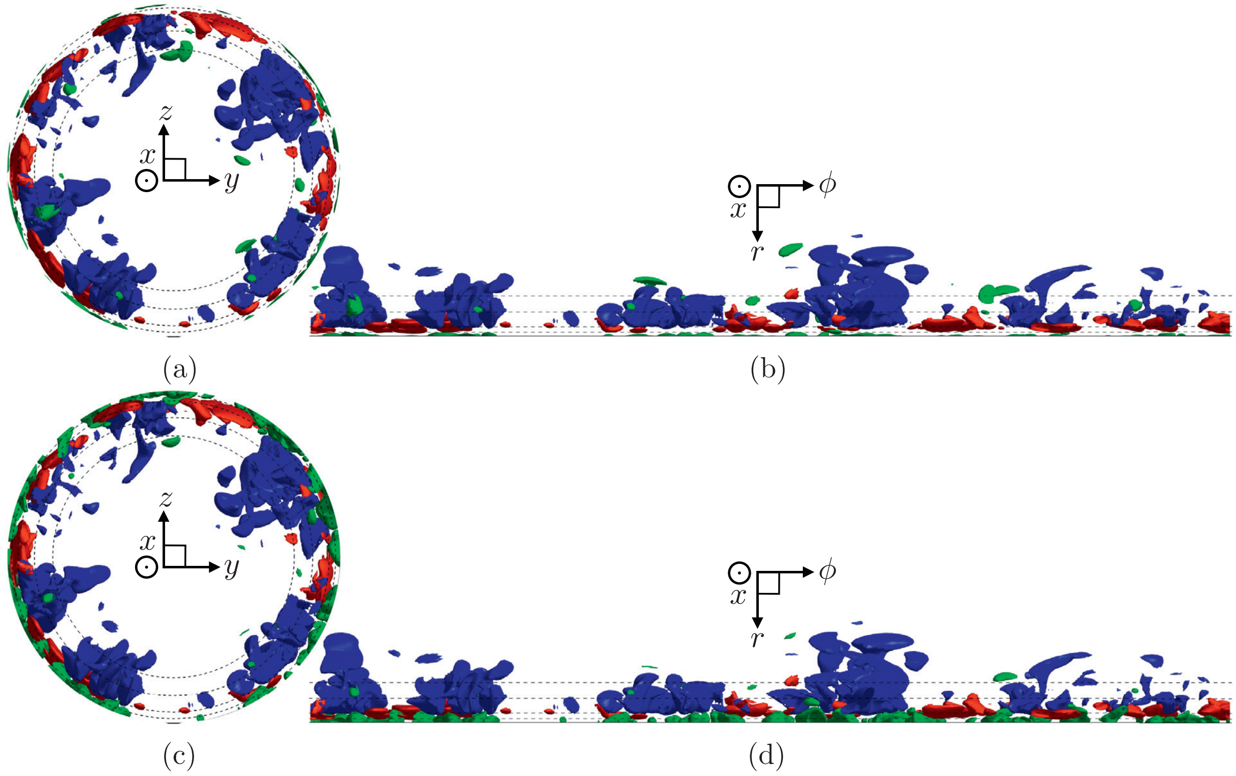

(a) (b)

(c) (d)

Fig. 7. Same as in Fig. 6 but different viewpoint (vortical structures are omitted for clarity of the remaining structures). On the top/bottom figure the LF/GF has been used for the computation of inactive structures. The flow direction is towards the reader. The continuous line represents the pipe wall, while the following dashed lines are placed at $(R-r)^+ = 5,\ 12,\ 30,\ 50$. (For interpretation of the references to color in this figure legend, the reader is referred to the web version of this article.)

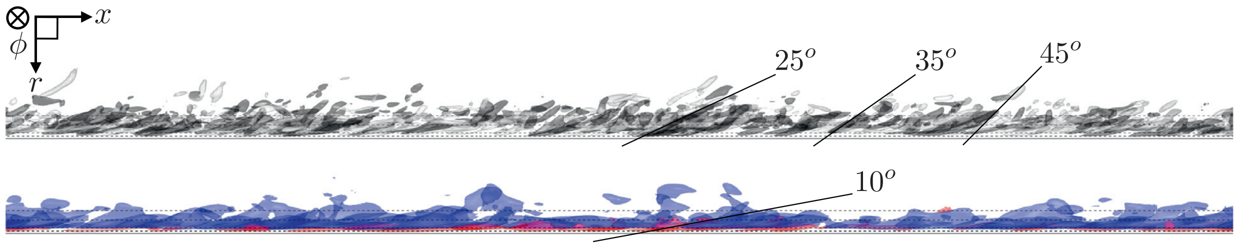

Fig. 8. Visualization of vortical/streaky structures in Cylindrical coordinate system (top/bottom). Translucency is used in order to observe all structures located at different circumferential locations. Inclination angles are shown on the structures. See also the details of Figs. 6 and 7. (For interpretation of the references to color in this figure legend, the reader is referred to the web version of this article.)

region $12 < (R-r)^+ < 30$. On the other hand, the inactive structures are mainly located close to the wall. The top/bottom part of Fig. 7 shows the inactive structures as computed via the LF/GF. Inactive structures computed via the LF occupy the region $(R-r)^+ < 5$, while inactive structures computed via the GF are located in the region $(R-r)^+ < 12$.

Representative inclination angles of streaks and vortices are shown in Fig. 8. It is evident that the streaks have lower inclination angles than the quasi-streamwise vortices. The inclination angle of streaks (more specifically of the low-speed streaks) are around 10^o, while for the quasi-streamwise vortices the inclination angle depends highly on the radial location of the structures. Later on, we will show that the inclination angles of the structures are in good agreement with the rotation angles that place the structure tensors in their principal axes (see discussion for Fig. 23).

To quantify the mean streamwise extent of the streaks and the mean separation between high-speed and low-speed streaks, Wu and Moin [56] used two-point correlations of the streamwise fluctuating velocity (Figs. 29, and 31 therein). Since we have not computed two-point correlations in our simulation, we use Fig. 9 to qualitatively compare with the data of Wu and Moin [56]. The visualizations and correlations of Wu and Moin [56] suggest that at $Re_\tau = 180$ turbulent pipe flow possesses large-scale, near-wall structures that are coherent over significant axial dimensions (8R or larger). This is in agreement with our data illustrated in Fig. 9.

According to the literature the mean separation between high-speed and low-speed streaks is about $\phi r^+ = 50 \sim 60$. Close to the wall the data of Wagner et al. [55] (Fig. 15 therein) indicate high-speed to low-speed streak azimuthal separation of $\phi r^+ \approx 60$. For channel flow at $Re_\tau = 180$, the near-wall data of Kim et al. [25] (Fig. 23 therein) indicate spanwise separation of $z^+ \approx 55$. This means that close to the wall there must be around 18 streaks (counting both high-speed and low-speed) along the azimuthal direction. Our data in Fig. 9 are in accordance to Wagner et al. [55] and Kim et al. [25].

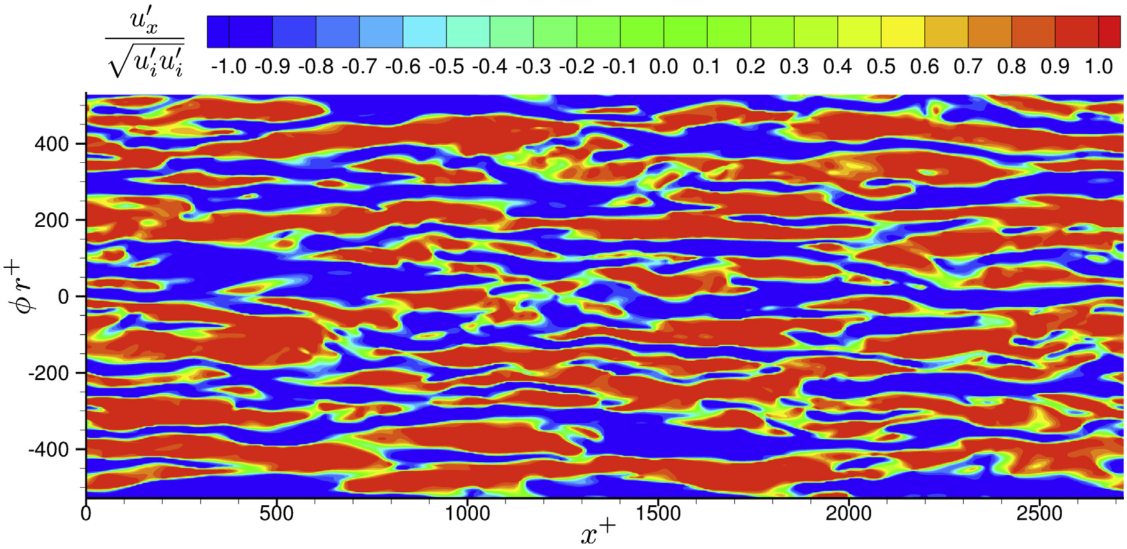

Fig. 9. Contour plot of the normalized streamwise fluctuating velocity component at $r = 0.9338R$ or $(R - r)^+ = 12$. The range of the horizontal axis is x: $[0, 15R]$ or x^+ : $[0, 2720]$, while the range of the vertical axis is $r\phi : (-0.9338\pi, +0.9338\pi]$ or $\phi r^+ : (-532, +532]$. Red/Blue color indicates regions of high/low-speed streaks. A rough estimation of the streamwise and circumferential extent of the streaks can be extracted from this figure. (For interpretation of the references to color in this figure legend, the reader is referred to the web version of this article.)

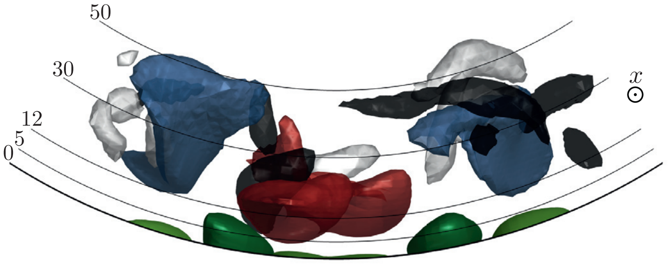

Fig. 10. A representative schematic of the various types of structures appearing in a turbulent pipe flow at $Re_b = 5300$. The wall is marked with a thick line while the rest of the lines are placed at $(R - r)^+ = 5, 12, 30, 50$. The streamwise direction is towards the reader. Two low-speed streaks and one high-speed streak are shown with blue and red color respectively. Vortical structures with right/left hand rotation around the positive x-axis are shown with gray/black color. Inactive structures predicted by the LF/GF are illustrated with light/dark green color. (For interpretation of the references to color in this figure legend, the reader is referred to the web version of this article.)

4.4. A representative schematic of the structures

The figures of this section highlight the spatial organization of a representative collection of structures located in the viscous wall region, and allow one to understand the interaction taking place among the various types of structures. To assist the reader we provide in the electronic supplementary material a viewpoint animation of the schematics of Figs. 10–12.

We begin with the well-known quasi-streamwise vortices, which have been observed both experimentally [45] and numerically [25]. The vortical structures of Fig. 10 are colored based on their streamwise rotational sense; i.e. gray/black color corresponds to right/left hand rotation around the streamwise direction. For further understanding, Fig. 11a shows the wrapping of fluctuating velocity lines around the vortical structures, which is in agreement with the rotational sense of these structures. In the pipe circumferential direction, the vortical structures are organized with alternating sense of streamwise rotation. Any such pair of counter-rotating vortices acts as a redistribution engine, either sending high-speed fluid towards the wall, thus generating a high-speed streak, or ejecting low-speed fluid further away from the wall, thus generating a low-speed streak. As a result of the splatting events high-speed streaks are located closer to the wall, having higher extend in the circumferential direction than in the radial. On the other hand, the ejection events place the low-speed streaks somewhat further away from the wall, giving them a higher extend in the radial direction than in the circumferential.

According to Fig. 11b the areas directly under the streaks have the same sign of fluctuating streamwise velocity as with the streaks. Taking into account the no-slip condition on the wall, the fluctuating vorticity vectors become tangent to the wall and a dominant circumferential fluctuating vorticity component is anticipated in the areas directly under the streaks. Furthermore, as shown in Fig. 12b, the areas directly under a high/low-speed streak must have a positive/negative circumferential fluctuating vorticity. The opposite must hold for the areas directly above the streaks. Therefore, directly under and above the streaks, the radial component of the fluctuating vorticity remains small compared to the circumferential component. However, any two neighboring high-speed and low-speed streaks tend to organize the fluid between them, generating significant radial fluctuating vorticity. The sign of the generated radial fluctuating vorticity depends on the circumferential arrangement of the streaks, and thus alternates in sign as one moves in the circumferential direction. Low-speed/high-speed pairs of streaks generate positive radial fluctuating vorticity in their in-between region, while high-speed/low-speed pairs generate negative radial fluctuating vorticity. The combined effect of all previous comments explains the wrapping of fluctuating vorticity lines around the streaks demonstrated in Fig. 12a.

We proceed with the newly defined inactive structures. In Figs. 10–12 the inactive structures predicted by the LF/GF are illustrated with light/dark green color. According to the GF, the adjacent to the wall inactive structures are located in areas between the streaks, where the fluctuating vorticity field is reorganized from a wall-tangent mode to a wall-normal orientation. Based on Fig. 10 the shape of the GF inactive structures is leaning towards the side of low-speed streaks. Fig. 12b shows clearly how the GF inactive structures act as organizers of the near-wall fluctuating vorticity field. In their periphery, which reaches below the streaks, the fluctuating vorticity vectors are tangent to the wall and primarily aligned with the circumferential direction. Only

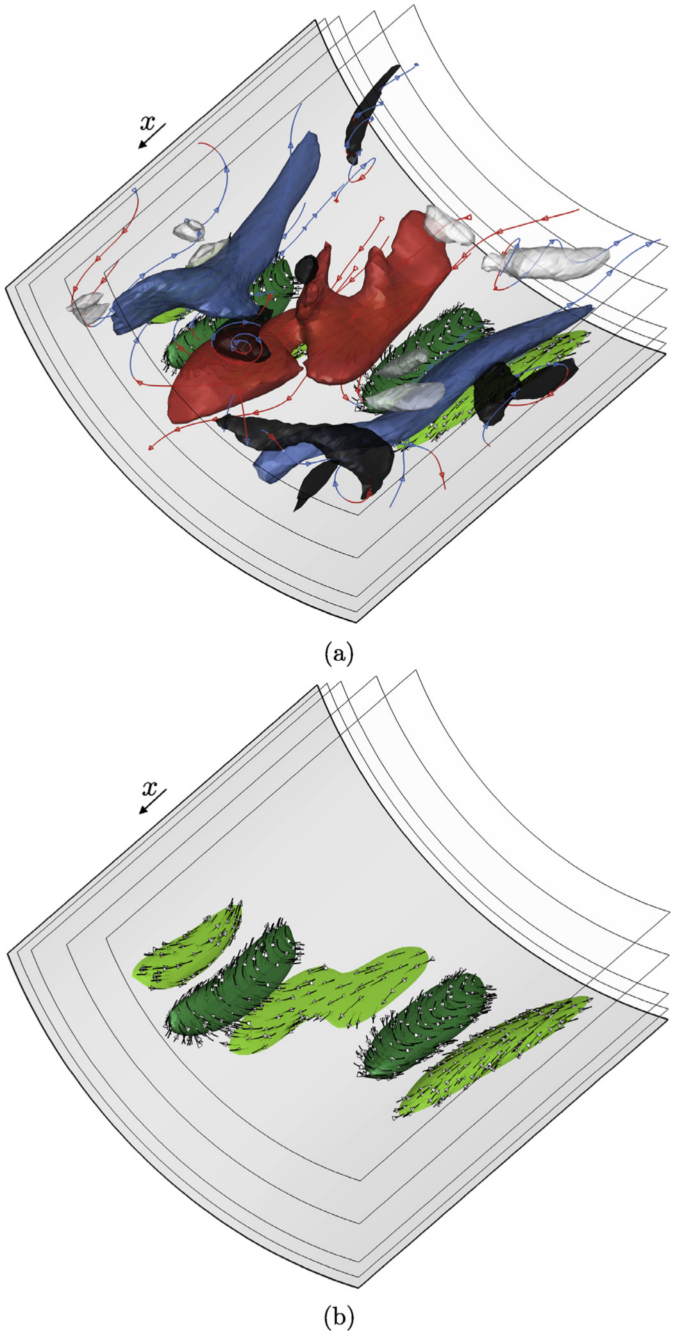

Fig. 11. Same as in Fig. 10 but different viewpoint. In addition fluctuating velocity lines are shown in the near region of the structures. Short fluctuating velocity lines with black color are attached to the inactive structures. The fluctuating velocity lines with blue/red color indicate negative/positive local streamwise fluctuating velocity component. The bottom part of the figure illustrates only the inactive structures and their associated fluctuating velocity lines. Note that the pipe wall is illustrated with gray color. (For interpretation of the references to color in this figure legend, the reader is referred to the web version of this article.)

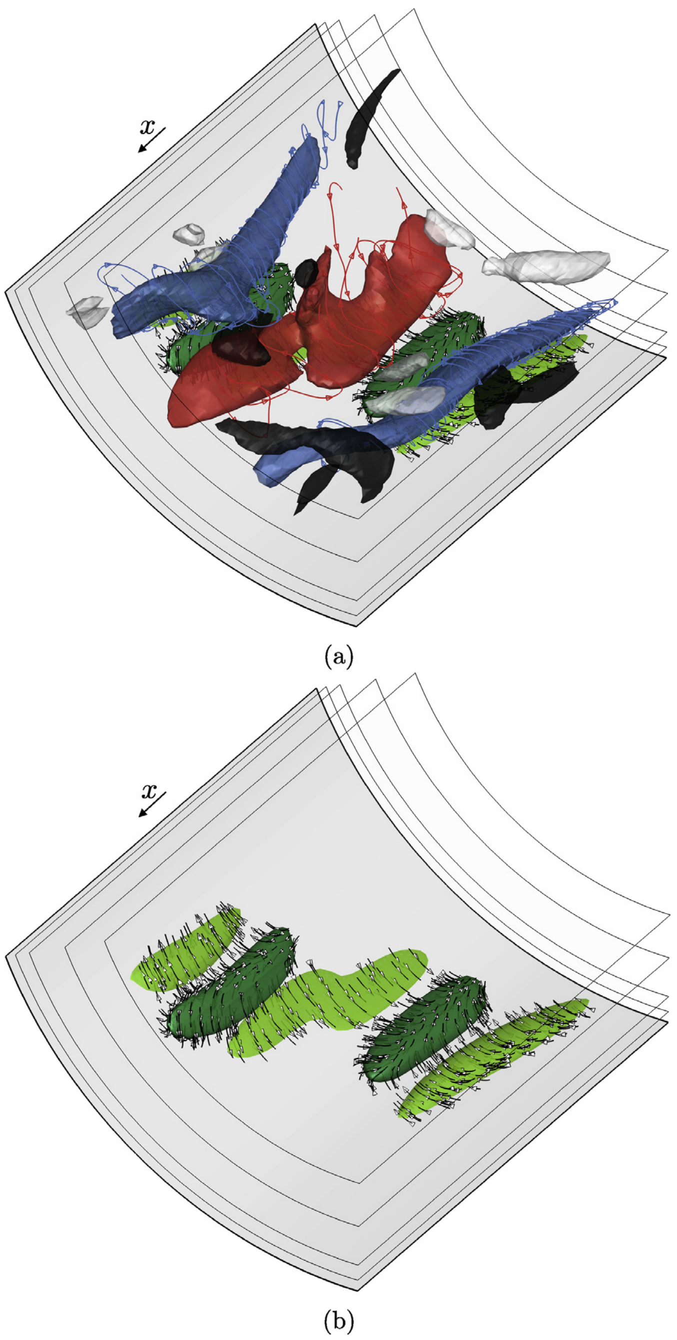

Fig. 12. Same as in Fig. 10 but different viewpoint. In addition fluctuating vorticity lines are shown in the near region of the structures. Short fluctuating vorticity lines with black color are attached to the inactive structures. The fluctuating vorticity lines with blue/red color indicate negative/positive local streamwise fluctuating velocity component. The bottom part of the figure illustrates only the inactive structures and their associated fluctuating vorticity lines. Note that the pipe wall is illustrated with gray color. (For interpretation of the references to color in this figure legend, the reader is referred to the web version of this article.)

the head and tail of these structures have a streamwise fluctuating vorticity component. The central region of these structures extends to higher distances from the wall and has primarily wall-normal fluctuating vorticity. The sign of the fluctuating vorticity vector depends on the circumferential arrangement of the streaks. A low-speed/high-speed pair of streaks generates fluctuating vorticity lines splatting towards the wall, while a high-speed/low-speed pair produces fluctuating vorticity lines ejecting from the wall. Finally, we note that the organization of the vorticity in the inactive structures is associated with a velocity field that lies primarily in the wall-tangential plane.

According to the LF, the adjacent to the wall inactive structures are located exactly below the streaks. Based on Fig. 10 the radial extend of these structures is very small. Fig. 11 reveals a coherent unidirectional character for the fluctuating velocity lines along the LF inactive structures, in the same direction with the one of the streaks just above them. The same holds for the fluctuating vorticity as Fig. 12 indicates. The poor choice of the LF boundary gauge

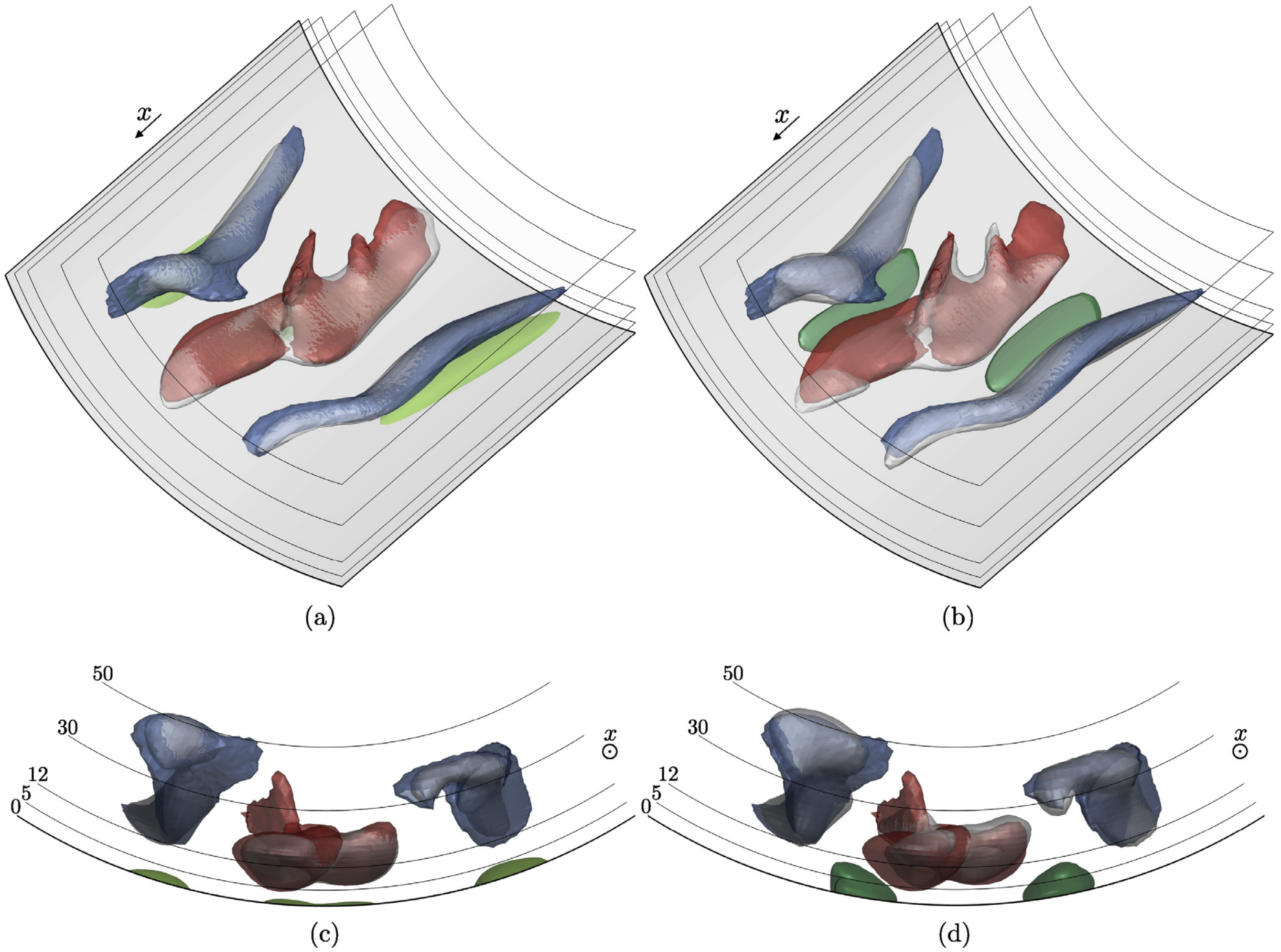

Fig. 13. Side view (a,b) and front view (c,d) of a representative pipe section (with length $\Delta L_x = 1.37R$ and angle $\Delta\phi = 65^o$) illustrating different types of structures appearing in a turbulent pipe flow at $Re_b = 5300$. In (a,c)/(b,d) the LF/GF has been used for the construction of the $Q^{\psi'}$-based structures. The streaks, one high-speed (red color) and two low-speed (blue color), are constructed from iso-surfaces of high turbulent kinetic energy values $k^t \gg 0$. Gray translucent structures correspond to $Q^{\psi'} \gg 0$, while green structures correspond to $Q^{\psi'} \ll 0$. (For interpretation of the references to color in this figure legend, the reader is referred to the web version of this article.)

condition, breaks the link between the vorticity and stream vector as one approaches the wall. As a result, the LF inactive structures represent merely the footprint of the streaks on the wall. They fail to bring to focus the localized organization of the fluctuating vorticity field that takes place in-between the streaks.

Animation of structures in time reveals that the inactive structures are always located in areas below the streaks (i.e. they travel with the same speed as the streaks). For this reason we have named the GF inactive structures as *"vorticity crawlers"* to highlight their roll as spatial organizers of fluctuating vorticity, and to emphasize the fact that they move on the wall. On the other hand, we have named the LF inactive structures as *"streak shadows"*, for obvious reasons.

So far, we have paid attention to $Q^{\psi'} < 0$ as a criterion for identifying vorticity crawlers and streak shadows. However, $Q^{\psi'} > 0$ is also a useful diagnostic as it captures the active structures, i.e. the large-scale structures that contribute directly to the turbulent kinetic energy. Therefore, the instantaneous iso-surfaces of $Q^{\psi'}$ can be used to differentiate between active and inactive structures. For example, Fig. 13 highlights the spatial organization of a representative set of structures located in the viscous near-wall region, extending from the wall to $y^+ \lesssim 50$. Two different criteria are used for the visualization of structures. The first corresponds to high values of the turbulent kinetic energy k^t, while the second to either positive or negative values of $Q^{\psi'}$. High values of k^t identify locations of high-speed and low-speed streaks, shown with red and blue color respectively. These are located in the region $5 \lesssim y^+ \lesssim 50$. In the same range, positive values of $Q^{\psi'}$, illustrated with translucent gray color, coincide with the areas of high k^t values. Evidently, $Q^{\psi'} > 0$ captures the near-wall streaks. This holds true for both LF (Fig. 13a,c) and GF (Fig. 13b,d). Of course, below $y^+ \lesssim 5$, negative values of $Q^{\psi'}$ (shown in green color) identify regions with "inactive structures" already discussed.

5. One-point turbulence structure tensors

In the previous section, we have examined the near-wall structures using both standard visualization criteria, such as the $Q^{u'}$ and k^t, as well as the newly introduced $Q^{\psi'}$-criterion. Having in mind the picture of the near-wall structures, we now proceed to report the associated profiles of the one-point structure tensors. The structure tensors have been previously reported in a DNS of fully-developed turbulent channel flow by Grigoriadis et al. [13] and Kassinos et al. [21] using only the LF. Recently, Vartdal [52] has used the GF to compute the profiles of the structure tensors in fully-developed channel flow, which he compared to the profiles generated via the LF. The focus of his work was on the difference between the two frameworks. The connection between the structure tensor profiles and the structures of turbulence was not addressed.

In this section, we report for the first time the one-point structure tensors in a fully-developed turbulent pipe flow and we extract the information carried by them. We demonstrate how the profiles of the structure tensors capture the key features of the large-scale near-wall structures. We use both the LF and GF to compute the structure tensors, and we demonstrate the superiority of GF over LF in describing effectively the coherent structures of turbulence. In the figures that follow, lines with/without cross symbols represent computation using the LF/GF. We report both the unnormalized and normalized structure tensors, but we discuss mainly the normalized ones. The normalization removes the strong dependence on the local turbulent kinetic energy level and brings to focus the inter-component relationships, thus leading to a clearer physical interpretation.

5.1. Alternative implementations and error estimates

The calculation of the structure tensors can follow two alternative routes. One can either use their definitions or use appropriate contractions of the third-rank tensor Q_{ijk}. Analytically the two approaches are equivalent, but numerically they involve different levels of numerical error. The two approaches are described by the relations

$$R^{u'}_{ij} = \overline{u'_i u'_j} \qquad R^{Q}_{ij} = \epsilon_{imp} Q_{mjp} \tag{36}$$

$$D^{\psi'}_{ij} = \overline{\psi'_{n,i}\psi'_{n,j}} \qquad D^{Q,C}_{ij} = \epsilon_{imp} Q_{pmj} + C^{\psi'}_{ij} \tag{37}$$

$$F^{\psi'}_{ij} = \overline{\psi'_{i,n}\psi'_{j,n}} \qquad F^{Q,C}_{ij} = \epsilon_{imp} Q_{jpm} + C^{\psi'}_{ji}\,. \tag{38}$$

For the calculation of the inhomogeneity and the third-rank tensors we use

$$C^{\psi'}_{ij} = \overline{\psi'_{i,n}\psi'_{n,j}} \qquad Q_{ijk} = -\overline{u'_j\psi'_{i,k}}. \tag{39}$$

The calculation of the inhomogeneity is unique, whereas for the calculation of the third-rank tensor one can either use Eq. (39) or the second half of Eq. (8). Here, we have used only Eq. (39) because it can be shown to provide better accuracy, owing to the fact that the velocity is identically zero on the wall.

In the remaining part of this subsection, we use the alternative methods given above to compute the first invariants of the structure tensors. This allows us to compare the corresponding levels of numerical error in the stream vector computation. Once this is established, in the following subsections we proceed to use the most accurate method to compute the remaining profiles of the structure tensors.

The first invariants of the structure tensors are of great significance. These invariants are important ingredients in turbulence modeling and they are used to normalize the structure tensors. Fig. 14 depicts the first invariant of the componentality, dimensionality, circulicity, and inhomogeneity tensors. The non-zero contractions of the stropholysis tensor are also presented. A single method has been used for the computation of the stropholysis tensor contractions. For the calculations of the first invariants of the Reynolds stress, dimensionality, and circulicity, we use the two methods of Eqs. (36)–(38), while for the inhomogeneity we use the following three methods

$$\begin{aligned} C^{\psi'}_{kk} &= \overline{\psi'_{k,n}\psi'_{n,k}} \\ C^{\psi',u'}_{kk} &= D^{\psi'}_{kk} - R^{u'}_{kk} \\ C^{Q,C,u'}_{kk} &= D^{Q,C}_{kk} - R^{u'}_{kk}. \end{aligned} \tag{40}$$

Another possibility is to use: $C^{\psi',Q}_{kk} = D^{\psi'}_{kk} - R^{Q}_{kk}$, but we have confirmed numerically that it gives the same result as $C^{Q,C,u'}_{kk}$. The option $C^{Q,C,Q}_{kk} = D^{Q,C}_{kk} - R^{Q}_{kk}$ is redundant because analytically is the same with $C^{\psi'}_{kk}$.

Some important conclusions follow from Fig. 14. Considering the velocity-based calculation of the Reynolds stress $R^{u'}_{kk}$ as error-free, then the differences between $R^{u'}_{kk}$ and R^{Q}_{kk} give an indication of the level of the numerical errors in the stream vector computations. These errors are small throughout the pipe radius. The comparison for the computation of the inhomogeneity trace involves only three lines, since two of the four possible ways to calculate C_{kk} give the same results (as explained above). For this reason, we consider the $C^{Q,C,u'}_{kk}$ as the method with the lowest numerical errors. The two remaining methods give results that bound the values of $C^{Q,C,u'}_{kk}$, and thus again give an indication on the numerical errors. For the computation of dimensionality, we consider $D^{Q,C}_{kk}$ to be the most accurate method, since it satisfies numerically the identity $C_{kk} = D_{kk} - R_{kk}$ if the most accurate computations of the inhomogeneity and the componentality traces are substituted, namely $C^{Q,C,u'}_{kk}$ and $R^{u'}_{kk}$.

5.2. Interpretation of the invariants of the structure tensors

Examination of the tensor traces offers a valuable overview of the behavior of the structure tensors. For example, each of the stropholysis contractions is at least one order of magnitude smaller than the level of the second-rank tensor traces. The degree of inhomogeneity is large in the viscous wall region $(R-r)^+ < 50$. This is expected, and is attributed to the wall effects. The small (but non-zero) value of inhomogeneity in the outer layer is attributed to the gradually vanishing velocity gradient and to non-local effects that influence the pipe centerline region. In the log-law region, the inhomogeneity is almost zero, and thus the flow can be considered as locally homogeneous. The inhomogeneity invariant attains negative values, as allowed by the lack of positive semi-definiteness of C_{ij}, while the dimensionality and circulicity contractions are identical to each other and everywhere positive. This is always true in any flow and geometry as their definition implies. The Reynolds stress contraction (which is twice the turbulent kinetic energy) is of comparable size with the contraction of dimensionality (or circulicity), except very close to the wall. In general, at the wall the turbulent kinetic energy is always zero, while the dimensionality can have non-zero values. It is straight forward to show that at a wall $D^{wall}_{kk} = F^{wall}_{kk} = C^{wall}_{kk}$ and $R^{wall}_{kk} = 0$. Since the degree of inhomogeneity is always large at a wall, it follows that the first invariant of dimensionality or circulicity will be non-zero, rendering them more suitable for normalization purposes than the Reynolds stress invariant. We also note that the footprint of the inactive structures is reflected in the profile of C_{kk}, which becomes large and positive very close to the wall. Finally, it is worth noting the differences between the LF and GF results, especially in the region close to the wall, where the effect of the imposed boundary conditions is strongest. While the profiles are quite similar in the bulk of the flow, the near-wall differences can have important implication for the tuning of structure-based RANS closures (see Appendix B).

Next, we consider the profiles of the components of each of the structure tensors in light of the structure visualizations presented in Sections 4.3 and 4.4. In the discussion that follows, emphasis is placed on the structure tensor profiles obtained with the GF implementation, which we consider to be the superior choice. Where appropriate, differences between the LF-based and GF-based profiles are discussed.

5.3. Componentality tensor

In Fig. 15 we report the unnormalized and self-normalized Reynolds stress tensor. For the computation of the self-normalized

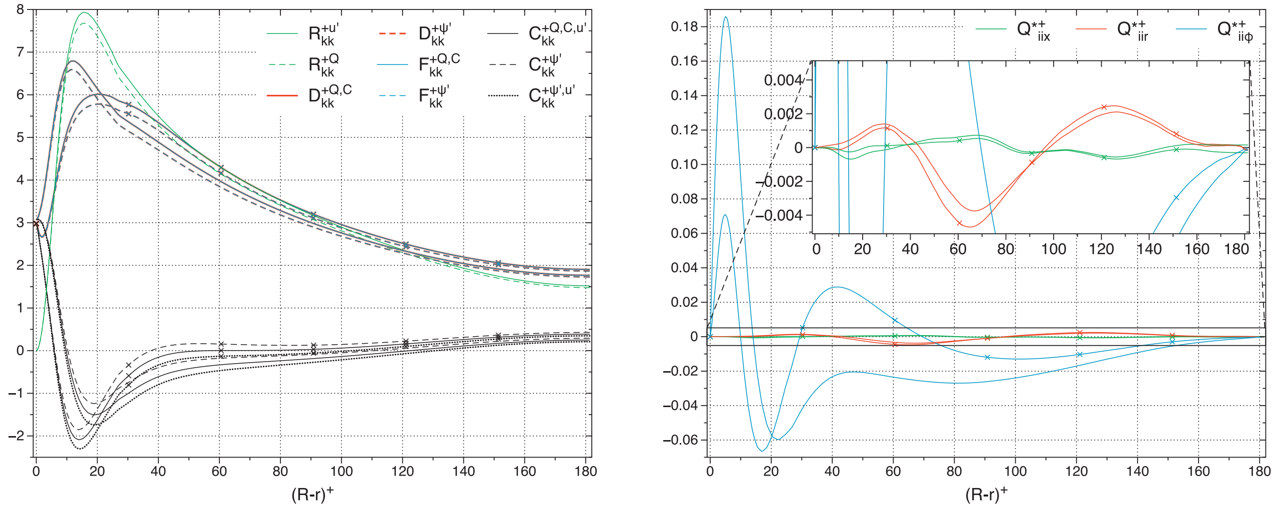

(a) (b)

Fig. 14. (a) First invariant of componentality Eq. (36), dimensionality Eq. (37), circulicity Eq. (38), and inhomogeneity Eq. (40). (b) Non-zero contractions of the stropholysis tensor Eq. (12). The results are normalized with wall units. Lines with/without cross symbols represent computation using the LF/GF.

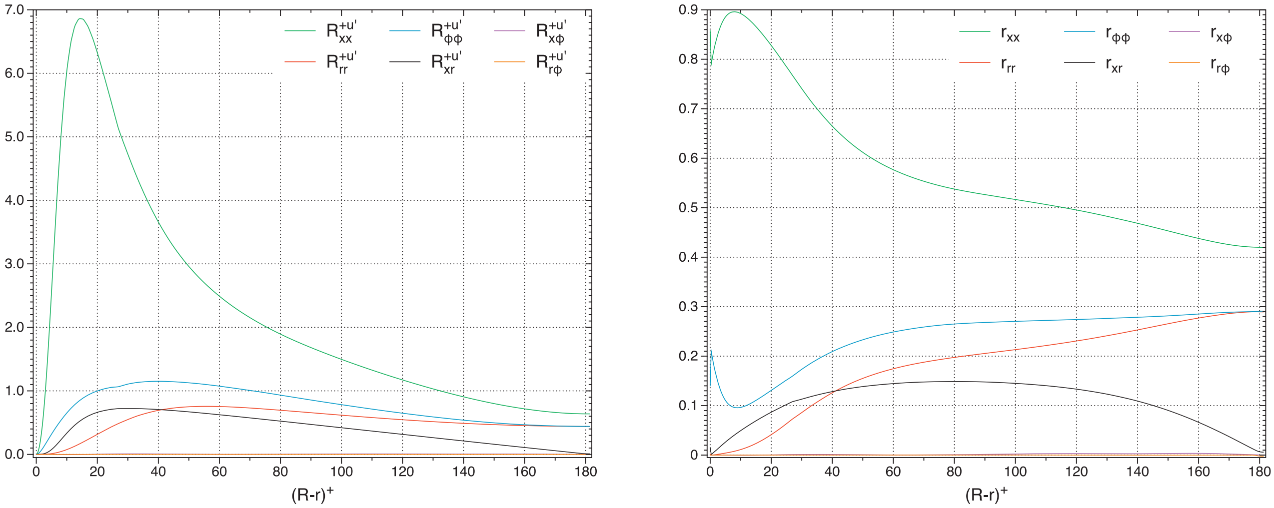

(a) (b)

Fig. 15. (a) Componentality tensor Eq. (36), normalized with wall units. (b) Self-normalized componentality tensor Eq. (41).

Reynolds stress tensor we use the following expression

$$r_{ij} = \frac{R^{u'}_{ij}}{R^{u'}_{kk}}. \tag{41}$$

The minuscule value of R_{kk} in the proximity of the wall gives rise to distinct cusps in the profiles of r_{ij} that should be disregarded (i.e. division by zero). The shear stress r_{xr} is zero at the wall and at the centerline, which results in a zero production at the same locations. Since the Reynolds stress is a measure of the componentality, it is evident that at the wall the flow is two component (2C), while away from the wall the flow is three component (3C). At the centerline, r_{rr} and $r_{\phi\phi}$ are indistinguishable.

Using a Taylor series expansion for the fluctuating velocity components near the wall, it can be shown [38] that r_{xx} and $r_{\phi\phi}$ attain non-zero values, while r_{rr} and r_{xr} attain zero values with a quadratic and linear functional form respectively,

$$r_{xx} = (1-\alpha) + \beta\tilde{r} - \gamma\tilde{r}^2 + \mathcal{O}(\tilde{r}^3) \tag{42}$$

$$r_{rr} = (\gamma - \gamma')\tilde{r}^2 + \mathcal{O}(\tilde{r}^3) \tag{43}$$

$$r_{\phi\phi} = \alpha - \beta\tilde{r} + \gamma'\tilde{r}^2 + \mathcal{O}(\tilde{r}^3) \tag{44}$$

$$r_{xr} = \beta''\tilde{r} - \gamma''\tilde{r}^2 + \mathcal{O}(\tilde{r}^3), \tag{45}$$

where $\tilde{r} = 1 - r/R$, the constants are all positive, $\gamma > \gamma'$, and $\alpha < 0.5$. These trends are captured correctly in Fig. 15. The no-slip boundary condition and the viscous forces in the near-wall region, drive the tangential components of velocity to zero. The inviscid wall blocking mechanism, which acts at distances far larger than the viscous effects, drives the wall normal velocity component to zero faster. In the near-wall region, the energy-containing structures that dominate, are high-speed and low-speed streamwise streaks. Since the energy is concentrated mainly on the streamwise fluctuating velocity component, r_{xx} is considerably larger than the $r_{\phi\phi}$. The near-wall maximum of r_{xx} (and therefore the minimum of $r_{\phi\phi}$) can be explained by the maximum of the shear rate parameter at the same location [28].

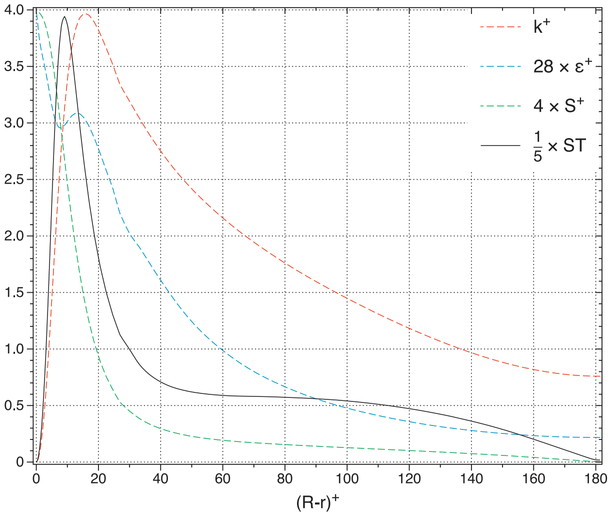

Fig. 16. Turbulent kinetic energy k, pseudo dissipation ϵ, shear rate S, and shear rate parameter ST as a function of the distance form the wall. The maximum value of the shear rate parameter $ST = 19.75$ is located at $(R-r)^+ = 9$.

Fig. 16 shows the profiles of the turbulent kinetic energy $k = \frac{1}{2}\overline{u_i' u_i'}$, pseudo dissipation $\epsilon = \nu \overline{u_{i,j}' u_{i,j}'}$, shear rate $S = -\frac{d u_x}{dr}$, and shear rate parameter $ST = S\frac{k}{\epsilon}$. The shear rate parameter is a dimensionless parameter that compares the eddy turnover time $T = \frac{k}{\epsilon}$, to the time scale of mean deformation $\frac{1}{S}$. High values of the shear rate parameter correspond to regions of high Reynolds stress anisotropy. For example, both ST and the Reynolds stress anisotropy attain their maximum values at around $(R-r)^+ = 9$ (see Figs. 15 and 16), while both drop as one moves away from this radial position.

Lee et al. [28] compared instantaneous structures and statistical correlations between homogeneous shear flow and an inhomogeneous channel flow at comparable high shear rate parameters. They found considerable similarities: coherent motions consisting of regions of low-speed and high-speed fluid (streaks), elongated in the streamwise direction and alternating in the shear/spanwise direction. They conjectured that (a) high shear rate produces structures in homogeneous turbulence similar to the streaks that are present in wall-bounded turbulent shear flows, and (b) high shear rate alone is sufficient for generation of streaky structures, and that the presence of a solid boundary is not necessary. Because of the high shear rate, rapid distortion theory (RDT) predicts remarkably well the anisotropic behavior of the normalized Reynolds stress tensor at $(R-r)^+ \approx 9$. When the shear rate parameter is large $ST \gg 1$, the large-scale structures of turbulence do not have time to come into equilibrium with the mean flow. In this case the Reynolds stresses depend upon the total shear St, and thus the turbulence has a viscoelastic-like character. The appropriate theory in this limit is the RDT, where the turbulence-turbulence interactions are negligible; turbulence is affected mostly by the mean flow and not by the turbulence itself. To obtain the RDT anisotropy levels of the normalized Reynolds stress tensor we have used the Particle Representation Model (PRM) [19]. The PRM model is exact in the homogeneous inviscid RDT limit. For a homogeneous rapid plane shear mean flow (which corresponds to a mean deformation tensor $G_{ij} = \overline{u}_{i,j} = -S\delta_{i,1}\delta_{j,2}$) the PRM predictions are shown Fig. 17. The Reynolds stress components at $St = 19.75$ compare remarkably well with the respective values of Fig. 15 at $(R-r)^+ \approx 9$ corresponding to $ST = 19.75$. Lee et al. [28] showed similar agreement between channel flow and DNS of homogeneous rapid shear flow (note that the PRM was not developed back then). We will come back to Fig. 17 to discuss the dimensionality results.

Lee et al. [28] also observed that the shear rate in the logarithmic layer of wall-bounded turbulent flows compares well to the shear rate used in the slow homogeneous shear case in the DNS of Rogers and Moin [43]. In these simulations, the authors did not observe elongated streak-like structures, but instead found the presence of hairpin vortices. The identification of quasi-streamwise vortical structures in these studies is consistent with the trends in Fig. 15. Away from the rapid shear location $(R-r)^+ > 9$, the streamwise fluctuating velocity decreases while the secondary fluctuating velocities increase, indicating that the structures transition from a jetal to a vortical character as one moves away from the wall and into the logarithmic layer.

For comparison purposes between the normalized structure tensors, we adopt the first invariant of dimensionality as the common normalization factor. To this end we construct a second definition for the normalized Reynolds stress (distinguishable by the over-hat)

$$\hat{r}_{ij} = \frac{R_{ij}^{u'}}{D_{kk}^{Q,C}}. \tag{46}$$

In Fig. 18 we compare the normalized Reynolds stress $\hat{r}_{ij}$ as computed by LF and GF. Note that the normalization factor D_{kk} is solely responsible for the differences between the LF and GF. At the wall, all components drop to zero since the dimensionality normalization factor is non-zero. The dominant component of the Reynolds stress tensor is the R_{xx}, which corresponds to the fraction of turbulent kinetic energy found in streamwise fluctuations. When normalized by R_{kk} it attains its maximum value at $(R-r)^+ \approx 9$ (see Fig. 15), while when normalized by D_{kk} the location of the maximum shifts to $(R-r)^+ \approx 12$ for the LF, and to $(R-r)^+ \approx 17$ for the GF (see Fig. 18). Note that the strong streamwise jetal character prevails over the streamwise vortical character throughout the pipe radius ($r_{xx} \gg r_{rr}$, $r_{\phi\phi}$).

5.4. Inhomogeneity tensor

We proceed with the normalized inhomogeneity,

$$\hat{c}_{ij} = \frac{C_{ij}^{\psi'}}{D_{kk}^{Q,C}}. \tag{47}$$

Note, that $\hat{c}_{ij}$ is non-symmetric and thus all nine components are unique. The profiles of Fig. 19 give a measure of the relative importance of inhomogeneity effects throughout the pipe radius. Recasting the definition of inhomogeneity into the form $C_{ij} = (\overline{\psi_i' \psi_{k,j}'})_{,k}$ and noticing that for any set of i, j the summation index k will run over the radial inhomogeneous direction, we can expect non-zero values even for C_{xx} and $C_{\phi\phi}$ (i.e. the elements of inhomogeneity with indices in the purely homogeneous directions). This is in analogy with the flow field, where all velocity components (with homogeneous or inhomogeneous indices) are affected by the presence of the walls.

It has been shown by Kassinos and Reynolds [18], that at the wall $C_{ij}^{wall} = C_{ji}^{wall} = D_{ij}^{wall} = F_{ij}^{wall}$. One can easily prove these equalities by simply noticing that at the wall $\psi_{i,j}^{\prime wall} = \psi_{j,i}^{\prime wall}$ (i.e. the stream vector definition, along with the zero velocity at the wall imply this definition). The equality of inhomogeneity and dimensionality at the wall can help us understand why $\hat{c}_{xx}^{wall} \ll \hat{c}_{\phi\phi}^{wall} \lesssim \hat{c}_{rr}^{wall}$. As it has be shown through the visualizations, the near-wall inactive structures (i.e. vorticity crawlers and streak shadows) have large streamwise extent with a comparably small size in the circumferential and radial directions. The shape of these structures is described well by the dimensionality components as

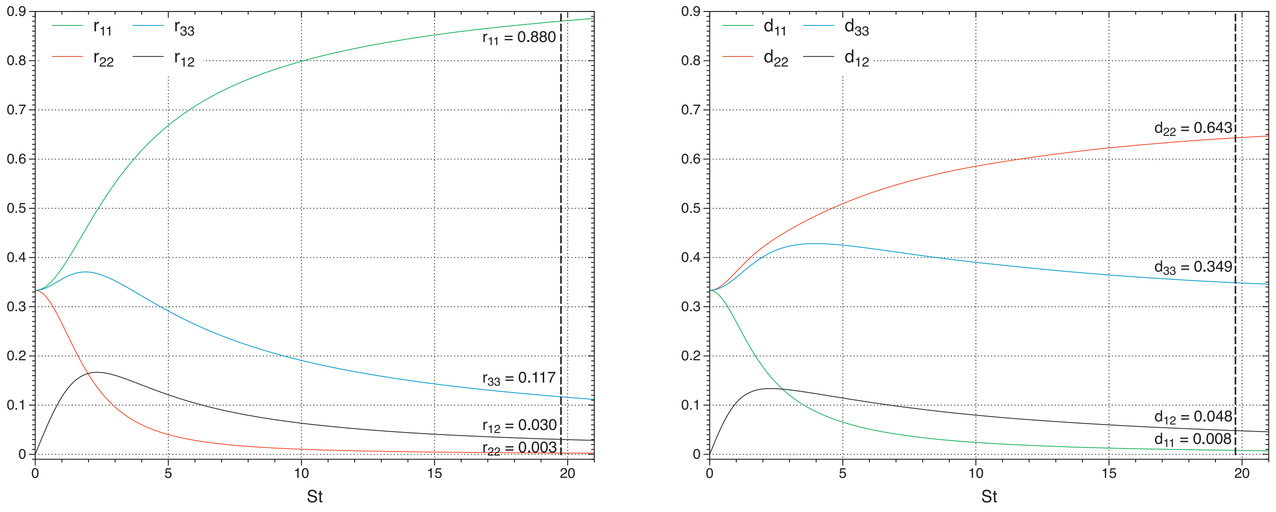

(a) (b)

Fig. 17. The PRM (which is exact in the homogeneous RDT limit) is used to obtain the evolution of the self-normalized (a) Reynolds stress and (b) dimensionality components. The case represents a homogeneous rapid plane shear mean flow which corresponds to the mean deformation tensor $G_{ij} = \overline{u}_{i,j} = -S\delta_{i,1}\delta_{j,2}$. Isotropic state is used as initial condition for the Reynolds stress and dimensionality tensors. The vertical dashed lines are located at total shear $St = 19.75$, same as the maximum value of the shear rate parameter in the current DNS pipe flow.

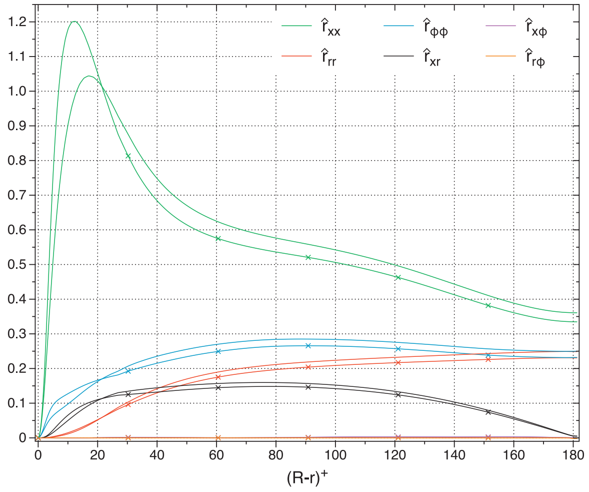

Fig. 18. Componentality tensor normalized by the first invariant of dimensionality Eq. (46). Lines with/without cross symbols represent computation using the LF/GF.

$\hat{d}^{wall}_{xx} \ll \hat{d}^{wall}_{\phi\phi} \lesssim \hat{d}^{wall}_{rr}$ (see the next subsection), and this explains the inhomogeneity values at the wall.

According to Kassinos and Reynolds [18] and Kassinos et al. [21], it can be shown analytically that $\hat{c}^{center}_{rr} = \hat{c}^{center}_{\phi\phi}$ at the pipe centerline, and that $\hat{c}^{wall}_{rr} = \hat{c}^{wall}_{\phi\phi} + \hat{c}^{wall}_{xx}$ at the wall. This is consistent with the computational results of Fig. 19. As expected, $\hat{c}_{rr}$ and $\hat{c}_{\phi\phi}$ are large in the near-wall region $(R-r)^+ < 30$, indicating a strong degree of inhomogeneity. At the pipe centerline small levels of inhomogeneity persist, which can be attributed to the gradual vanishing of the shear rate parameter ST as the pipe centerline is approached (see Fig. 16). A gradual change of the shear rate parameter mimics a near-wall region.

It is easier to appreciate the relative importance of the near-wall and centerline inhomogeneity values by looking at the unnormalized profiles of Fig. 19a. We note that when using LF/GF, $C^+_{rr} = C^+_{\phi\phi} \approx 0.215/0.153$ at the centerline, while $C^+_{rr} \approx 1.488/1.533$, $C^+_{\phi\phi} \approx 1.416/1.448$ at the wall. The trends of the unnormalized profiles of inhomogeneity are similar with the normalized ones. It is noteworthy that, in the adjacent to the wall region, the LF leads to a sharper and stronger local minimum than what GF leads to. Also, on average, the values obtained via LF have higher levels than the ones obtained by GF. These effects are attributed to the unphysical boundary conditions of LF which introduce inhomogeneous residuals.

It is important to point out the almost zero inhomogeneity in the log-law region, which indicates that the flow will have locally homogeneous characteristics. Local homogeneity in the log-region has been noted in the past, for example by Rogers and Moin [43]. The inhomogeneity tensor provides a quantitative measure of this effect. The approximate vanishing of $\hat{c}_{ij}$ means that in the log-region one-point statistics, like R_{ij}, D_{ij} and F_{ij}, satisfy constitutive equations normally associated with homogeneous turbulence. This is an important remark for turbulence modeling.

5.5. Dimensionality tensor

For the computation of the normalized dimensionality we use the following relation

$$\hat{d}_{ij} = \frac{D^{Q,C}_{ij}}{D^{Q,C}_{kk}}, \tag{48}$$

and in Fig. 20 we compare the LF and GF results. The various types of structures that are prevalent in a specific region of a turbulent flow provide a distinct contribution to the instantaneous dimensionality components. For example, an elongated structure aligned with a specific direction will have a small value for the corresponding dimensionality component. The statistical signature of the structures will in general be imprinted on the averaged one-point dimensionality tensor as well, which describes the directions of statistical independence of the turbulence. As is evident from Fig. 20, over the entire pipe radius the streamwise component $\hat{d}_{xx}$ is smaller than $\hat{d}_{rr}$ and $\hat{d}_{\phi\phi}$, indicating the existence of structures that are preferentially elongated in the streamwise direction.

As previously indicated, the maximum shear rate parameter $ST = 19.75$ corresponds to the radial location $(R-r)^+ = 9$. At this

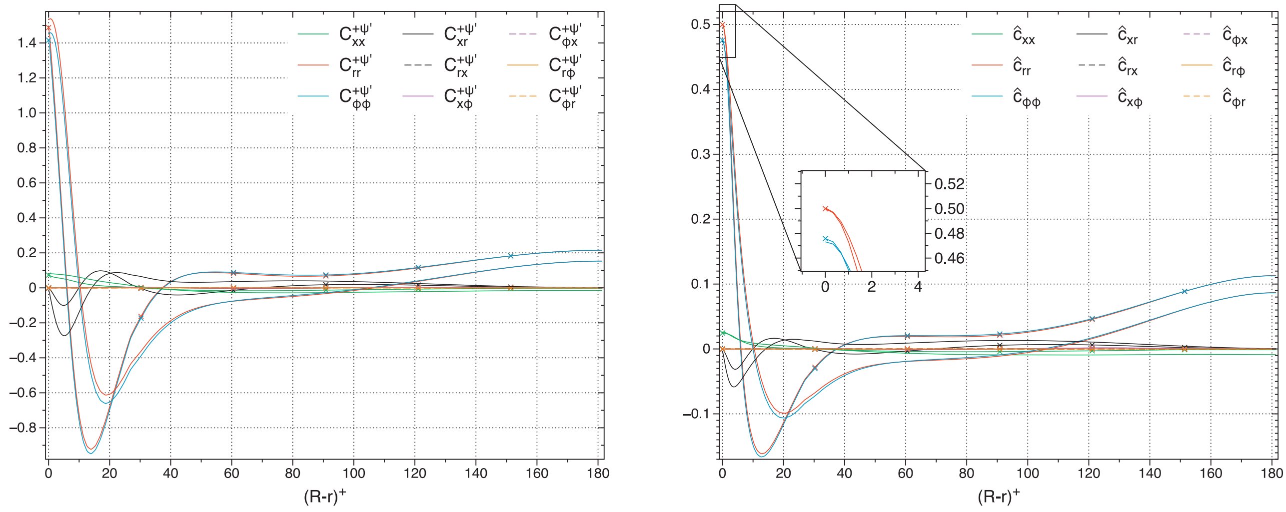

(a) (b)

Fig. 19. (a) Inhomogeneity tensor Eq. (39), normalized with wall units. (b) Inhomogeneity tensor normalization by the first invariant of dimensionality Eq. (47). Lines with/without cross symbols represent computation using the LF/GF.

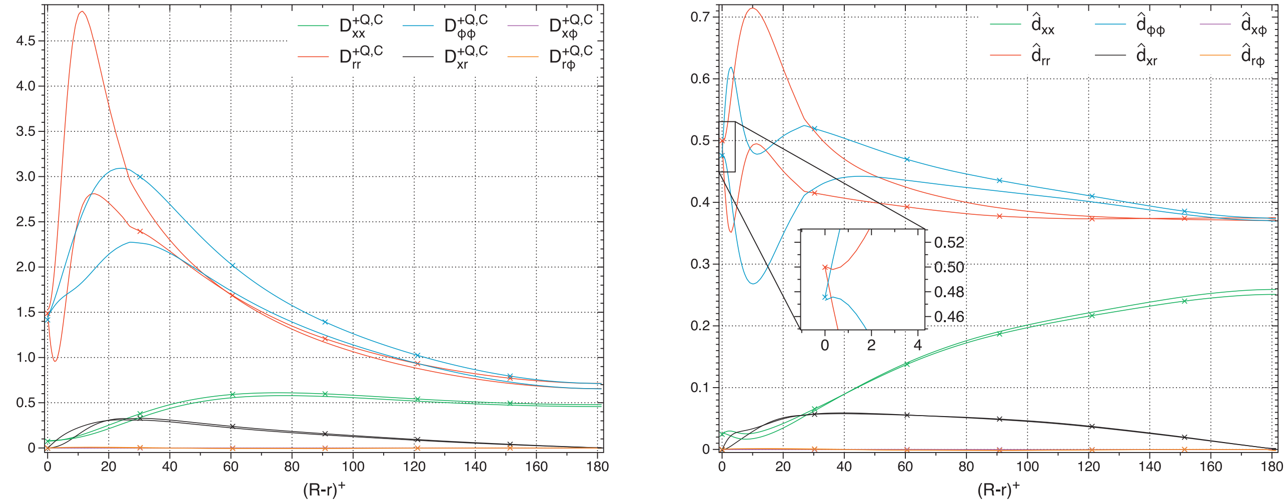

(a) (b)

Fig. 20. (a) Dimensionality tensor Eq. (37), normalized with wall units. (b) Self-normalized dimensionality tensor Eq. (48). Lines with/without cross symbols represent computation using the LF/GF.

radial location, RDT predicts remarkably well the levels of the self-normalized Reynolds stress components. The same holds true for the dimensionality. A comparison of the self-normalized dimensionality components at $(R-r)^+ = 9$ with the PRM predictions of Fig. 17, reveals that the results of GF are very close to the PRM predictions (this is not the case for the LF). Apparently, despite proximity to the wall, the morphology of the structures at the location of maximum *ST* is strikingly similar to that obtained under rapid homogeneous shear. The above comparison provides quantitative support to the qualitative observation that was first made by Lee et al. [28]. The implications for turbulence modeling are easy to imagine; for example, in structure-based models, RDT is used as guide for modeling the structure tensors even in inhomogeneous flows.

To further explain the GF profiles of Fig. 20, we divide the radial distance into regions according to the mapping of structures shown in Figs. 7 and 10. In the viscous sublayer $(R-r)^+ < 5$, the turbulent kinetic energy ($k = \frac{1}{2}R_{ii}$) attains its smallest values (see Fig. 14 or Fig. 16) and thus all scales collapse to the Kolmogorov and viscous scales. Therefore, the structure tensors in this region do not represent the active structures. Instead, as it has been shown earlier, positive values of C_{kk} indicate the existence of inactive structures. In the viscous sublayer $C_{kk} \approx D_{kk}$ (see Fig. 14). Thus, in this region, the dimensionality tensor reflects the shape of the inactive structures. As revealed by our visualizations, the near-wall inactive structures, i.e. the *vorticity crawlers*, tend to be long in the streamwise direction, fat in the azimuthal direction, and short in the radial direction. This description is consistent with the near-wall dimensionality values $\hat{d}^{GF}_{xx} \ll \hat{d}^{GF}_{\phi\phi} < \hat{d}^{GF}_{rr}$ of Fig. 20. In the case of LF, the near-wall dimensionality values $\hat{d}^{LF}_{xx} \ll \hat{d}^{LF}_{rr} < \hat{d}^{LF}_{\phi\phi}$ do not exactly describe the structural shape of the streak shadows. This inconsistency can be traced back to the boundary conditions used in the LF, which affect the dimensionality profiles over the entire pipe radius. Note though, that for $(R-r)^+ > 5$ (i.e. away from the source region of inactive structures) the trends of the dimensionality profiles between LF and GF are the same. When $\hat{d}_{ij}^{GF}$ increases or decreases the same does $\hat{d}_{ij}^{LF}$.

We proceed with the buffer layer $5 < (R-r)^+ < 30$. In this region, the turbulent kinetic energy obtains its maximum values and overtakes C_{kk}, and thus the dimensionality shows the structural shape of the active structures. In turbulent channel flow at $Re_\tau = 180$, quadrant analysis (see [25], Fig. 16 therein) reveals that $y^+ = 12$ is the point of equal prevalence of sweep and ejection events, with sweep events being dominant below and ejection events above this value. Since ejections and sweeps produce turbulent kinetic energy their signature is captured by the structure tensors. To explain the dimensionality profiles, we subdivide the buffer layer into two regimes: $5 < (R-r)^+ < 12$ and $12 < (R-r)^+ < 30$. In the regime of sweeps, high-speed fluid impinges towards the wall through the splatting process. The sweeps have the tendency to increase the circumferential extent of the high-speed streaks at the expense of reducing their radial extent. This explains the reduction of $\hat{d}_{\phi\phi}$ and the increase of $\hat{d}_{rr}$ in the regime of sweeps. On the other hand, in the regime of ejections, low-speed fluid is ejected away from the wall through the bursting process. The ejections have the tendency to increase the radial extent of the low-speed streaks at the expense of reducing their circumferential extent. This explains the increase of $\hat{d}_{\phi\phi}$ and the decrease of $\hat{d}_{rr}$ in the regime of ejections. Both high-speed and low-speed streaks have very long streamwise extent and this is imprinted in the low value of $\hat{d}_{xx}$.

Now that the bulk of the regimes $(R-r)^+ < 5$, $5 < (R-r)^+ < 12$, and $12 < (R-r)^+ < 30$ is understood, we concentrate on the transition points $(R-r)^+ = 5$, and $(R-r)^+ = 12$. Our visualizations show that vorticity crawlers have similar aspect ratios to that of high-speed streaks, with the latter having more profound structural anisotropy. This is consistent with the linear trends of GF profiles at $(R-r)^+ = 5$. As concerning the LF, our visualizations show that the high-speed and low-speed streaks in the region $(R-r)^+ > 5$ are always associated with inactive structures (i.e. streak shadows) that are placed with mirror symmetry in the region $(R-r)^+ < 5$. This explains the mirroring effect of $\hat{d}_{\phi\phi}^{LF}$ and $\hat{d}_{rr}^{LF}$ at $(R-r)^+ = 5$. Now at $(R-r)^+ = 10$ we observe, for both LF and GF, a local minimum for $\hat{d}_{\phi\phi}$ and a local maximum for $\hat{d}_{rr}$. These extrema are induced by the increasing occurrence of low-speed streaks in the area $(R-r)^+ > 12$, which have different shape than the high-speed streaks.

Note that $\hat{d}_{xr}$ is small but not exactly zero; this indicates that the streamwise extent of the streaks is slightly lifted up with respect to the wall. The rotation angle at each radial location needed to take the local dimensionality tensor to its principal axes, represents this inclination angle (see Fig. 23). In the range $5 < (R-r)^+ < 30$, the inclination angle θ is less than 10°. This is coincident with the shallow inclination angles of low-speed and high-speed streaks. Based on this analysis it is evident that the dimensionality tensor captures the structural features of the streaks.

As we enter the log-law region the $\hat{d}_{xx}$ increases to significant values. This indicates that the streamwise extent of the structures is significantly reduced. The difference between the $\hat{d}_{rr}$ and $\hat{d}_{\phi\phi}$ components is also reduced, giving evidence of structures with roughly circular cross-section. The inclination angle in the region $30 < (R-r)^+ < 100$ varies almost linearly between the values $8^o < \theta < 13^o$. This is consistent with the existence of quasi-streamwise vortices that have a smaller streamwise extent and higher inclination angles than the streaks. As we move further into the outer region $(R-r)^+ > 100$, the inclination angles start to drop till they reach a zero value at the pipe centerline. In this region, $\hat{d}_{xx}$ is only moderately lower than $\hat{d}_{rr}$ and $\hat{d}_{\phi\phi}$. This structural signature is consistent with the presence of large-scale turbulent bulges in the outer layer of turbulent flows.

5.6. Circulicity tensor

For the normalized circulicity we use the following relation

$$\hat{f}_{ij} = \frac{F_{ij}^{Q,C}}{D_{kk}^{Q,C}}, \tag{49}$$

and in Fig. 21 we compare the LF and GF results. To explain the profiles of Fig. 21 we divide the radial distance into the same regions as used for the examination of dimensionality. In the viscous sublayer $(R-r)^+ < 5$, where all scales collapse, the circulicity describes the inactive structures. According to the visualizations of Fig. 12, vorticity crawlers are characterized by weak streamwise and equally strong radial and azimuthal fluctuating vorticity. This coherent vorticity of crawlers is identified by the circulicity as $\hat{f}_{xx}^{GF} \ll \hat{f}_{\phi\phi}^{GF} \approx \hat{f}_{rr}^{GF}$. In the case of LF, the near-wall circulicity values $\hat{f}_{xx}^{LF} \ll \hat{f}_{\phi\phi}^{LF} < \hat{f}_{rr}^{LF}$ are not consistent with the fluctuating vorticity characterization of streak shadows (see Fig. 12). This is attributed to the poor choice of the LF boundary gauge condition, which breaks the link between the vorticity and stream vector. The mirroring effect of $\hat{f}_{\phi\phi}^{LF}$ and $\hat{f}_{rr}^{LF}$ at $(R-r)^+ = 5$, is attributed to the streaks and their associated streak shadows. Nevertheless, for $(R-r)^+ > 5$ (i.e. away from the source region of inactive structures) the trends of the circulicity profiles between LF and GF are the same. When $\hat{f}_{ij}^{GF}$ increases or decreases the same does $\hat{f}_{ij}^{LF}$.

As previously indicated, the maximum shear rate parameter $ST = 19.75$ corresponds to the radial location $(R-r)^+ = 9$. As we have seen, at this radial location, RDT predicts remarkably well both the self-normalized Reynolds stress and dimensionality components. At the same radial location, the GF inhomogeneity invariant C_{kk} is zero, which indicates that the structure tensors satisfy constitutive equations normally associated with homogeneous turbulence, i.e. $C_{ij} = 0$, $D_{kk} = F_{kk} = R_{kk}$, and $r_{ij} + d_{ij} + f_{ij} = \delta_{ij}$. It is therefore not surprising that at $(R-r)^+ = 9$, the GF circulicity components also correlate very well with the PRM predictions (not shown).

The rapid change of the streamwise fluctuating velocity below the streaks, generates a high shear area with increased azimuthal fluctuating vorticity. For this reason, $\hat{f}_{\phi\phi}$ increases at the expense of $\hat{f}_{rr}$ in the first part of buffer layer, $5 < (R-r)^+ < 12$. On the other hand, the area between a pair of streaks is characterized again by high shear, but with increased radial fluctuating vorticity. This explains the increase of $\hat{f}_{rr}$ at the expense of $\hat{f}_{\phi\phi}$ in the second part of buffer layer, $12 < (R-r)^+ < 30$.

The rapid increase of $\hat{f}_{xx}$ in the buffer layer implies growth of streamwise circulation. The fluid motion around the quasi-streamwise vortical structures generates streamwise vorticity, which activates the $\hat{f}_{xx}$ component. The splatting and busting processes of streaks demands the existence of quasi-streamwise vortical structures, in order for the fluid to move away and towards the wall. This agrees with the high values of $\hat{f}_{xx}$ away from the pipe wall. It is clear that $\hat{f}_{xx}$ is an effect of streamwise vortical structures, while $\hat{f}_{rr}$ and $\hat{f}_{\phi\phi}$ are an effect of streamwise streaks. We can argue that the streaks are more energetic than the vortices since $\hat{f}_{xx} < \hat{f}_{\phi\phi}, \hat{f}_{rr}$.

The non-zero value of $\hat{f}_{xr}$ indicates that the axis of the streamwise vortices is actually lifted up and at an angle relative to the wall; this justifies the use of the term *"quasi-streamwise vortices"*. The rotation angle at each radial location needed to take the local circulicity tensor to its principal axes, represents this inclination angle (see Fig. 23). For the LF the inclination angle θ increases linearly between the values $7^o < \theta < 25^o$ for the radial distances

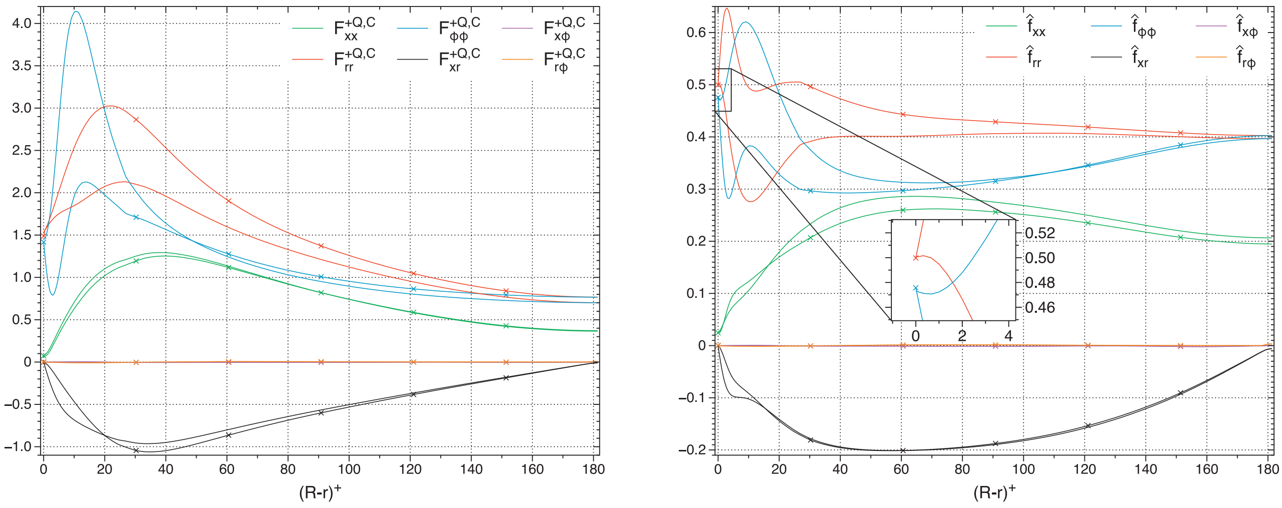

(a) (b)

Fig. 21. (a) Circulicity tensor Eq. (38), normalized with wall units. (b) Circulicity tensor normalization by the first invariant of dimensionality Eq. (49). Lines with/without cross symbols represent computation using the LF/GF.

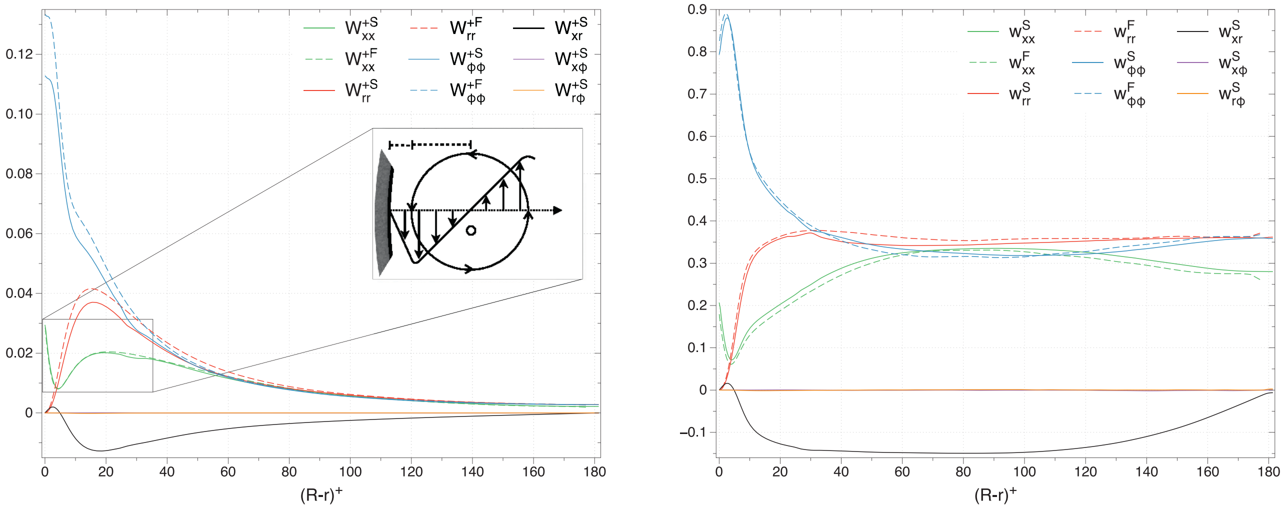

(a) (b)

Fig. 22. (a) Vorticity tensor normalized with wall units. (b) Self-normalized Vorticity tensor. Comparison between our data (denoted by "S") and the data of Fukagata and Kasagi [12] (denoted by "F"). The subfigure is adopted from the work of Kim et al. [25] (Fig. 15 therein) and represents the average location of the quasi-streamwise vortices from the wall. The rotational direction is such that the streamwise fluctuating vorticity is positive. The opposite rotational direction has equal probability of appearance.

$5 < (R-r)^+ < 30$. In the range $30 < (R-r)^+ < 70$, the inclination angle increases again monotonically (but at a slower rate) between the values $25^o < \theta < 33^o$. The inclination angle drops in the range $(R-r)^+ > 70$. For the GF the inclination angles are $5^o \sim 10^o$ higher in the viscous wall region. As the centerline is approached the differences of the two frameworks become smaller. The angles of GF are in better agreement with the visualizations of Fig. 8.

5.7. Vorticity tensor

As already explained, the circulicity tensor represents the large-scale coherent circulation. For further understanding of circulicity tensor, we compare with the small-scale vorticity tensor. In Fig. 22, we report the non-normalized $W_{ij} = \overline{\omega_i'\omega_j'}$ and normalized $w_{ij} = \frac{W_{ij}}{W_{kk}}$ vorticity tensor components. Our data are compared with the data of Fukagata and Kasagi [12]. Note that they did not report the values for W_{xr}. While the data for W_{xx} are in good agreement at the wall, this is not the case for $W_{\phi\phi}$. At the wall $(\omega_x'^{wall})^2 = \left(\frac{\partial u_\phi'}{\partial r}\Big|_{r=R}\right)^2$ and $(\omega_\phi'^{wall})^2 = \left(\frac{\partial u_x'}{\partial r}\Big|_{r=R}\right)^2$, thus both vorticity components depend on radial derivatives. Our grid spacing normal to the wall is smaller than the one of Fukagata and Kasagi [12]. Also our circumferential spacing is smaller, and the streamwise extent of our domain is larger. All the previous comments indicate that our data should be more accurate than the data of Fukagata and Kasagi [12]. In any case, the normalized vorticity tensor components are in good agreement.

At the wall, it can be shown that $r_{xx}^{wall} = w_{\phi\phi}^{wall}$ and $r_{\phi\phi}^{wall} = w_{xx}^{wall}$. Our data satisfy these relations and thus they are consistent. Since $r_{xx}^{wall} > r_{\phi\phi}^{wall}$, the aforementioned relations indicate that $W_{\phi\phi}^{wall} > W_{xx}^{wall}$. The high value of $W_{\phi\phi}^{wall}$ is merely an effect of high streamwise fluctuating velocity shear generated between the wall and the streaks. The maximum of W_{rr} is located at $(R-r)^+ = 15$, exactly

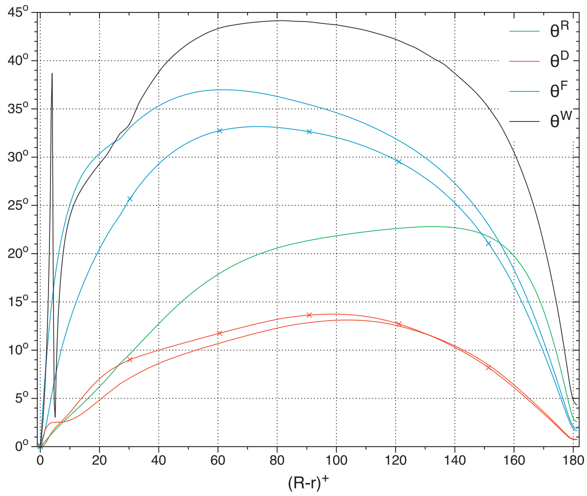

Fig. 23. The rotation angles θ^R, θ^D, θ^F, and θ^W, that transform respectively the $R_{ij}^{u'}$, $D_{ij}^{Q,C}$, $F_{ij}^{Q,C}$, and W_{ij} to their principal axes (based on right hand rotations around the positive ϕ-axis). Lines with/without cross symbols represent computation using the LF/GF.

where R_{xx} obtains its maximum value. This is not a coincidence since W_{rr} is an effect of shear generated in the region between adjacent high-speed and low-speed streaks. The computed results of W_{xx} show a local minimum at $(R-r)^+ = 5$ and a local maximum at $(R-r)^+ = 20$. Moser and Moin [34] attributed this behavior to the existence of streamwise vortices. As they explained the location of local maximum of W_{xx} corresponds to the average location of the center of streamwise vortices, while the local minimum is caused by the streamwise fluctuating vorticity with opposite sign created at the wall because of the no-slip boundary condition. To elaborate this we have included a subfigure schematic in Fig. 22. The schematic is adopted from Kim et al. [25] (Fig. 15 therein) and it represents a near-wall vortical structure. As Kim et al. [25] explain, in a single realization the streamwise fluctuating vorticity must become zero somewhere between the center of the vortex and the wall, but on the average its rms value would have a local minimum at the average location of the edge of the vortex. Therefore, the streamwise vortices are located at $(R-r)^+ = 20$ with radius $\rho^+ = 15$. In the outer layer $(R-r)^+ > 50$ the values of the unnormalized vorticity tensor components drop significantly.

We proceed with the normalized vorticity tensor. If we exclude the near viscous sublayer region $(R-r)^+ < 10$, the normalized vorticity tensor components w_{xx} and w_{xr} have a remarkable resemblance with the respective components of circulicity. The same holds true for the other two vorticity tensor components, w_{rr} and $w_{\phi\phi}$, which show a similar resemblance to the respective circulicity components, $\hat{f}_{rr}$ and $\hat{f}_{\phi\phi}$ (at least for the GF). This is interesting since one would think of w_{ij} as being a small-scale quantity and of f_{ij} as being large-scale. The fact that the two behave similarly indicates that the streamwise vortical eddies have strong coherence across scales. This explains why small-scale velocity gradient based criteria, such as the $Q^{u'}$, $\lambda_2^{u'}$, and $\Delta^{u'}$, are capable of identifying coherent vortices which are also found in visualizations from other large-scale high-energy based methods, such as the Proper Orthogonal Decomposition analysis. As explained, in the near-wall viscous sublayer region, the circulicity tensor describes the inactive structures, while away from this region it characterizes the active structures. On the other hand, note that the vorticity tensor has a single meaning over the entire pipe radius (it represents the vorticity statistics). The ability of the circulicity to capture both types of structures (versus the single meaning of the vorticity) explains differences in the behavior of the two tensors in the near-wall viscous sublayer region.

5.8. Rotation angles to principal axes

Fig. 23 compares the rotation angles, that transform the respective tensors to their principal axes, as a function of the distance from the wall. A non-zero rotation angle is obtained whenever the *xr* component of a tensor is non-zero. These angles give a measure of the mean inclination angle (from the wall) of the associated structures.

We note a sharp change in θ^W at $(R-r)^+ \approx 5$, which happens because near this radial location the components W_{xx} and W_{rr} change their relative relation. However, away from this particular location, θ^W and θ^F have similar radial functional forms and comparable value and this is consistent with the notion of coherence across scales that was introduced above. The rotation angles that place the structure tensors in their principal axes are in good agreement with the inclination angles of the structures (see Fig. 8). Specifically, the rotation angle θ^D correlates well with the low inclination angles of the streaks, while the rotation angle θ^W agrees with the inclination angles of the quasi-streamwise vortices.

5.9. Homogenized tensors

The one-point structure tensors contain the average structural information of turbulence and thus are well-suited for one-point turbulence modeling. In turbulence models, such as the ASBM, the homogenized tensors D_{ij}^{cc} and F_{ij}^{cc} are modeled directly since little is known on how to model C_{ij} in general flows. The homogenized tensors can be calculated by the gradients of the stream vector Eq. (7), or using the third-rank tensor Eq. (10). The method that involves the third-rank tensor proves to be more accurate (i.e. at the wall the *rr* and $\phi\phi$ components are exactly zero only for the aforementioned method). To this end we use the following normalizations

$$\hat{d}_{ij}^{cc} = \frac{D_{ij}^{cc\,Q}}{D_{kk}^{Q,C}} \tag{50}$$

$$\hat{f}_{ij}^{cc} = \frac{F_{ij}^{cc\,Q}}{D_{kk}^{Q,C}}. \tag{51}$$

Fig. 24 shows the profiles of these normalized homogenized tensors. Their wall values are zero (same as $\hat{r}_{ij}$) and they have the same trace with the Reynolds stress: $D_{kk}^{cc} = F_{kk}^{cc} = R_{kk}$. The only drawback of these modified tensors is that their diagonal components can become negative, since they are no longer positive semi-definite. In fact, this is the case for $\hat{d}_{rr}^{cc}$ and $\hat{f}_{\phi\phi}^{cc}$ as computed with the LF in the region $(R-r)^+ < 5$. It is interesting to note that this does not happen for the GF. This is another indication that the GF is more appropriate for turbulence modeling than the LF. For example, in the ASBM model the diagonal components of the homogenized tensors are built such that they are never negative.

5.10. Stropholysis tensor

Another important structure tensor is the stropholysis tensor Q_{ijk}^{*}. It contains information on the turbulence structure that is not included in the other second-rank tensors. It is a crucial ingredient for modeling the rapid pressure-strain tensor appearing in the Reynolds stress evolution equations. It is intimately connected with the effects of mean and frame rotation. Poroseva et al. [39] developed a Structure-Based turbulence Model (namely the Q-model) using the stropholysis tensor. It was found that this model is able to predict accurately the turbulent flow in a pipe at various

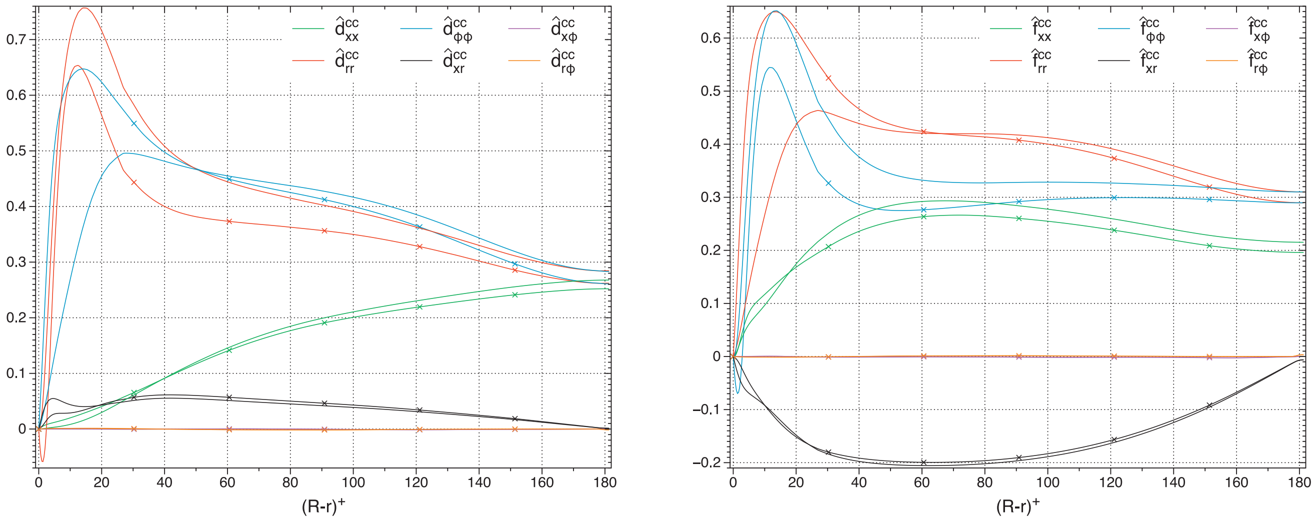

(a) (b)

Fig. 24. (a) Homogenized dimensionality tensor normalization by the first invariant of dimensionality Eq. (50). (b) Homogenized circulicity tensor normalization by the first invariant of dimensionality Eq. (51). Lines with/without cross symbols represent computation using the LF/GF.

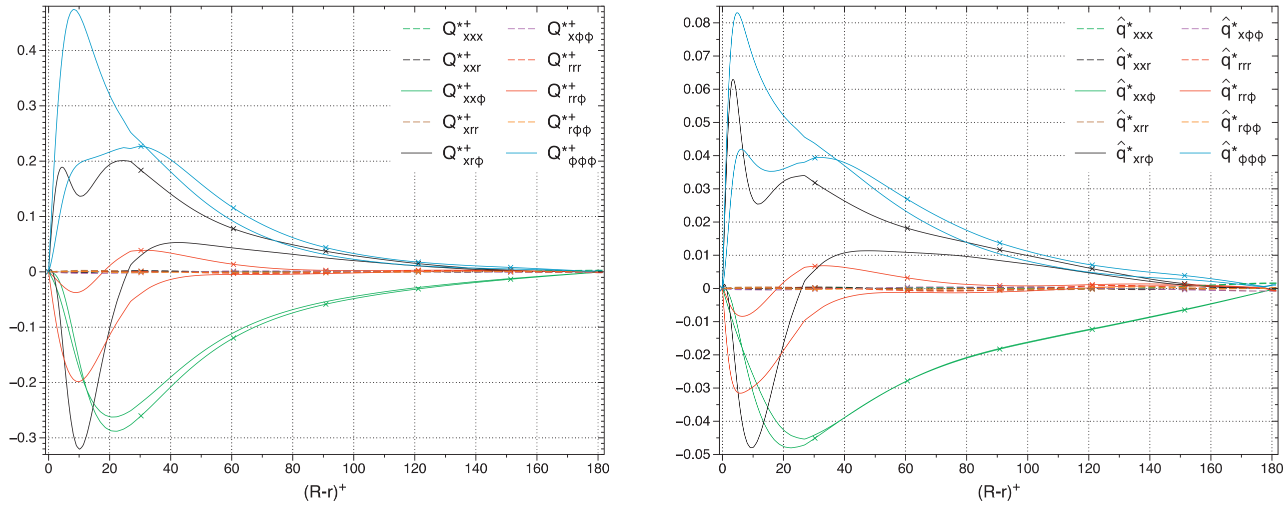

(a) (b)

Fig. 25. (a) Stropholysis tensor Eq. (12), normalized with wall units. (b) Stropholysis tensor normalized by the first invariant of dimensionality Eq. (52). Lines with/without cross symbols represent computation using the LF/GF.

Reynolds numbers and under stronger rotation than what is possible with the Reynolds Stress Transport Models (RSTMs). For further development of the Q-model the profiles of the stropholysis tensor are needed. For this reason, in Fig. 25 we report the profiles of the normalized stropholysis tensor

$$\hat{q}^*_{ijk} = \frac{Q^*_{ijk}}{D^{Q,C}_{kk}}. \tag{52}$$

Only $\hat{q}^*_{xx\phi}$, $\hat{q}^*_{rr\phi}$, $\hat{q}^*_{\phi\phi\phi}$, $\hat{q}^*_{xr\phi}$, out of the nine independent components of the fully symmetric $\hat{q}^*_{ijk}$, are significantly energized. The maximum value of the $\hat{q}^*_{ijk}$ tensor is one order of magnitude smaller than the maximum values of the second-rank structure tensors. The non-zero components of $\hat{q}^*_{ijk}$ contribute to the rapid pressure-strain-rate term. Note that the $\hat{q}^*_{xx\phi}$ is roughly equal to the negative of $\hat{q}^*_{\phi\phi\phi}$, which indicates a transfer of energy from $R_{\phi\phi}$ to R_{xx} (for more details and explanation see [21]). Note that the profiles obtained via the GF have a simpler functional form than the ones obtained via the LF. This signifies less effort in modeling the stropholysis tensor under the GF.

6. Conclusions and future plans

We have used Direct Numerical Simulations, along with our recently developed computational framework for the calculation of the fluctuating stream vector [48], to compute the one-point turbulence structure tensors in a fully-developed turbulent pipe flow at bulk Reynolds number $Re_b = 5300$. We demonstrated that the one-point structure tensors lack gauge invariance, and therefore, that the proper choice of a gauge is very important for the interpretation of the tensors. We have shown that the boundary gauge choice made in the General Framework preserves the meaning attached to the structure tensors under homogeneous turbulence arguments. In this sense, the General Framework is superior to the Limited Framework, used in earlier studies, and leads to a more meaningful interpretation of the structure tensor profiles in near-wall flows.

We have introduced a new structure identification criterion based on the second invariant of the fluctuating stream vector gradient ($Q^{\psi'} \equiv -\frac{1}{2}\psi'_{i,j}\psi'_{j,i}$) that allows extraction of large-scale structures with either very low or very high turbulent kinetic energy content. Using this criterion we have identified the *"vorticity crawlers"*. These are large-scale structures of low turbulent kinetic energy content that populate the region below the high-speed and low-speed streaks. They are localized in the spanwise (circumferential direction) in the areas in-between the streaks. Vorticity crawlers move with the same speed as the streaks and they correspond to regions below the streaks where the vorticity field is reorganized from wall-tangential alignment to a wall-normal orientation. The wall-normal alignment can be of positive or negative sign depending on the pair of streaks (high-speed - low-speed or low-speed - high-speed). Thus, vorticity crawlers correspond to events in the vorticity field that are caused by the combined action of near-wall streak pairs; these vorticity events mimic the splatting and ejection events in the velocity field that take place at higher distances from the wall, as result of the combined action of vortex pairs. Thus, one can think of a yin-yang sequence of events: the vortex structures organizing the velocity below them and then the velocity structures organizing the vorticity field just below *them*. The identification of the vorticity crawlers in the region $y^+ \leq 10$ completes the picture of the near-wall and extreme-near-wall structures. In the past, the near-wall strong radial variation of the one-point structure tensors could only be attributed loosely to the effect of boundary conditions. The emerging view of large-scale structure organization near the wall allows a more precise interpretation of the tensor profiles.

Apart from its significance for flow visualization, the identification of inactive structures (i.e. vorticity crawlers) is important for the near-wall implementation of structure-based models (SBMs), and we expect that it will lead to improvements in the near-wall treatment in SBMs, such as the ASBM. For this purpose, we are currently carrying fresh simulations designed to identify the separate contributions of active and inactive structures to the near-wall values of the Reynolds stresses and the other one-point structure tensors [47]. For this purpose, we are utilizing conditional averaging based on the newly derived Q^{ψ}-criterion. We suspect that accounting for the presence of the vorticity crawlers could lead to improved near-wall RANS closures in general. Furthermore, a very interesting application of the $Q^{\psi'}$-criterion, would be to use the numerical databases of square [37] and rectangular [54] turbulent duct flows, and try to further pinpoint the mechanisms responsible for the formation of Prandtl's secondary flow of second kind. RANS models based on the Boussinesq approximation are unable to predict such secondary flows, which have an important effect in a wide range of industrial applications. SBMs able to account for the formation of these secondary flows would be of great relevance to the community.

Finally, we stress that the current work has been performed in the context of low turbulent Reynolds numbers. This choice was driven by our interest in developing SBMs to be used for the prediction of pulmonary airflow in the human lungs, which is classified in the regime of low turbulent Reynolds numbers. The application of our $Q^{\psi'}$-criterion at much higher Reynolds numbers is certainly in our interests. In this direction, we have initiated Direct Numerical Simulations using the 6th-order compact finite difference cylindrical code of Boersma [4,5]. Clearly, the comparison between the low- and high-Reynolds number flows will provide valuable information for the near-wall structure-based turbulence modeling. In addition, at the high Reynolds numbers it will be interesting to describe the profiles of the structure tensors, in light of the vortex clusters (velocity gradient discriminant based structures) of del Álamo et al. [8] and the Q events (Reynolds shear stress based structures) of Lozano-Durán et al. [31], as well as their evolution in time [30].

Acknowledgments

This work is dedicated to the late Professor William C. Reynolds whose ideas continue to inspire our own.

This work has been supported by the US Army International Technology Center and the US Air Force European Office of Aerospace Research and Development (EOARD) under grant W911NF-11-1-0425. Partial support was also received under the contract of association (Contract No. ERB 5005 CT 99 0100) between the European Atomic Energy Community and the Hellenic Republic.

We would like to acknowledge the authors of El Khoury et al. [11] for kindly sharing with us the DNS results from their simulations. The DNS data of Wu and Moin [56] are available at https://ctr.stanford.edu/research-data , while the DNS data of Eggels et al. [10] and Fukagata and Kasagi [12] are available at http://thtlab.jp/DNS/dns_database.html.

The first author wishes to express his sincere gratitude to Prof. Dimokratis Grigoriadis for his insightful comments throughout this project.

Supplementary materials

Video clips and high resolution figures made available online at 10.1016/j.compfluid.2016.10.010.

Appendix A. Pressure gradient controller

To simulate a fully-developed turbulent pipe flow, it is standard practice to assume periodicity at the inlet and outlet part of the considered finite pipe geometry. In doing so, a driving force (namely the pressure gradient) must be specified in order to put energy into the system. Without this term the fluid is stagnant. There are two methods on how to specify the pressure gradient: either (a) by simply setting it as a constant number in order to fix the mean wall shear stress, or (b) by adjusting it in time in order to keep the volumetric flow rate constant.

The first method leads to a constant turbulent Reynolds number (or Kármán number)

$$Re_\tau = \frac{u_\tau R}{\nu} \tag{A.1}$$

where u_τ is the friction velocity

$$u_\tau = \sqrt{\frac{\tau_w}{\rho}} \qquad \tau_w \equiv -\nu\rho \frac{d\overline{u_x}}{dr}\bigg|_{r=R} = -\frac{1}{2}R\frac{d\overline{p_w}}{dx}. \tag{A.2}$$

The above equation relates the time averaged wall shear stress in the streamwise direction τ_w, with the time averaged pressure gradient at the wall $\frac{d\overline{p_w}}{dx}$, in the fully-developed state. However, one needs a method to obtain an estimate of τ_w. For a turbulent pipe flow, the mean velocity profile is approximated by von Kármán's "log-law" relation

$$\frac{\overline{u_x}(r)}{u_\tau} \approx \frac{1}{0.41}\ln\left(\frac{u_\tau(R-r)}{\nu}\right) + 5.0\,, \tag{A.3}$$

from which only approximate expressions, relating the pressure drop to the bulk velocity u_b or the bulk Reynolds number Re_b, can be extracted,

$$\frac{u_b}{u_\tau} \approx \frac{1}{0.41}\ln(Re_\tau) + 1.34 \tag{A.4}$$

$$\begin{aligned} \frac{1}{\sqrt{f_{turb}}} &\approx 2.00\log\left(0.40Re_b\sqrt{f_{turb}}\right) \\ f_{turb} &\equiv -\frac{d\overline{p_w}}{dx}\frac{D}{\frac{1}{2}\rho u_b^2} = \frac{32Re_\tau^2}{Re_b^2} \end{aligned} \tag{A.5}$$

$$Re_b \approx 11.31Re_\tau\log(2.25Re_\tau). \tag{A.6}$$

The second equation is Prandtl's friction law for smooth pipes. For a given Re_b (which corresponds to a specific u_b), one can use Eq. (A.6) to obtain an approximate value for Re_τ. Then for given values of ρ, ν, and R, Eqs. (A.1) and (A.2) determine the pressure drop in the pipe. However, the procedure described so far does not enforce a constant bulk velocity.

In this study we have used the second method, which leads to a constant bulk Reynolds number

$$Re_b = \frac{u_bD}{\nu} \tag{A.7}$$

where $D = 2R$ is the diameter of the pipe, R is the radius, and u_b is the bulk velocity

$$\begin{aligned} u_b &= \overline{u_b(t)} \\ u_b(t) &= \frac{1}{\pi R^2L_x}\int_0^{L_x}\int_0^{2\pi}\int_0^R u_x(t,x,r,\phi)rdrd\phi dx. \end{aligned} \tag{A.8}$$

The direction x of the coordinate system is along the pipe axis, and L_x is the length of the pipe. The overbar represents the time average process.

To make sure that the real time bulk velocity of the turbulent pipe flow is equal to (with small variations) the reference value, we have developed a Proportional Integral Derivative (PID) controller. At the end of each time step, the controller adjusts appropriately the value of the pressure drop, in order to keep the bulk velocity equal (or at least around) the reference bulk velocity. In the rest of this section, we explain how the pressure gradient is adjusted during the simulation time in order to keep the bulk velocity constant and consequently the Re_b fixed at 5300.

The PID controller is defined by the equation

$$\begin{aligned} \frac{1}{\rho}\frac{d}{dx}p_w(t) &= K_Pe(t) + K_I\int_0^t e(\tau)d\tau + K_D\frac{d}{dt}e(t) \\ e(t) &= u_b^{ref} - u_b(t) \end{aligned} \tag{A.9}$$

where $e(t)$ is the instantaneous deviation of the bulk velocity form the desired reference value u_b^{ref}, and K_P, K_D, K_I are tunable constants, namely the proportional, integral and derivative gains. Time discretization is used in the above equation to obtain the final form of the pressure gradient controller

$$\frac{1}{\rho}\frac{d}{dx}p_w(k) = \Pi_P(k) + \Pi_I(k) + \Pi_D(k) \tag{A.10}$$

$$\Pi_P(k) = K_Pe(k) \tag{A.11}$$

$$\Pi_I(k) = \Pi_I(k-1) + K_I\frac{\Delta t}{2}(e(k) + e(k-1)) \tag{A.12}$$

$$\Pi_D(k) = \frac{1}{1+N\Delta t}\left(\Pi_D(k-1) + K_DN\Delta t\frac{e(k)-e(k-1)}{\Delta t}\right), \tag{A.13}$$

where Δt is the time step of the simulation, k is the time step number, and N is the filter derivative coefficient. Using appropriate values for the parameters one can control the speed, stability and damping of the system. The integral part of the controller is important in order to give a zero steady state error (bulk velocity becomes equal to the reference value).

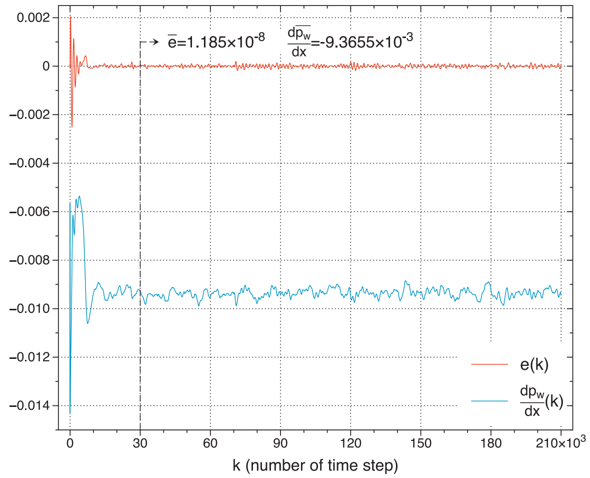

Fig. A1. Bulk velocity deviation from the reference value, and pressure gradient as calculated by the PID controller.

Recently, we have also implemented an alternative method based on the relation

$$\frac{1}{\rho}\frac{d}{dx}p_w(k) = -\frac{e(k-1)}{\Delta t} + \frac{2\nu}{R}\left\langle\frac{d}{dr}u_x(k-1)\bigg|_{r=R}\right\rangle, \tag{A.14}$$

where the brackets denote wall surface averaging. This is inspired by a similar approach reported in Veenman [53]. This relation is better grounded on physical arguments because it follows from taking the volumetric integral of the streamwise momentum equation and requiring $e(k) = 0$. Both approaches are successful in maintaining an essentially constant bulk velocity.

In our turbulent pipe simulation we have used the following values

$$\begin{aligned} &R = 1 \quad \rho = 1 \quad \nu = \frac{2}{5300} \quad u_b^{ref} = 1 \\ &\Rightarrow Re_b = 5300 \end{aligned} \tag{A.15}$$

$$\Delta t = 0.008 \quad (K_P, K_I, K_D) = (-0.5, -1.0, -2.0) \quad N = 30 \tag{A.16}$$

$$\Pi_D(0) = 0 \quad \Pi_I(0) = -\frac{2}{R}\tau_w = -2\rho\frac{(\nu Re_\tau)^2}{R^3}, \tag{A.17}$$

where an approximate value of 180 for Re_τ is obtained from Eq. (A.6) for $Re_b = 5300$. The values of K_P, K_D, K_I are empirically chosen for the specific $Re_b = 5300$. Note that since ρ, R and u_b have unit values, it follows that all results are automatically normalized by proper combinations of these variables.

In Fig. A.1 the pressure drop and the difference of the real time bulk velocity to the reference value are shown with respect to the number of time steps. In the first 6000 time steps an expected overshoot is shown. The small fluctuations of $e(k)$ after the dashed line are attributed partly to the finite length of the pipe, and partly to the inherent phase lag in the response of the bulk velocity to the applied pressure drop. The dashed vertical line denotes the starting point for the collection of statistics. Fig. A.1 shows also the average values of $e(k)$ and $\frac{dp_w}{dx}(k)$ over the range of 30,000–210,000 time steps

$$\bar{e} = 1.185\times10^{-8} \qquad \frac{d\overline{p_w}}{dx} = -9.366\times10^{-3}. \tag{A.18}$$

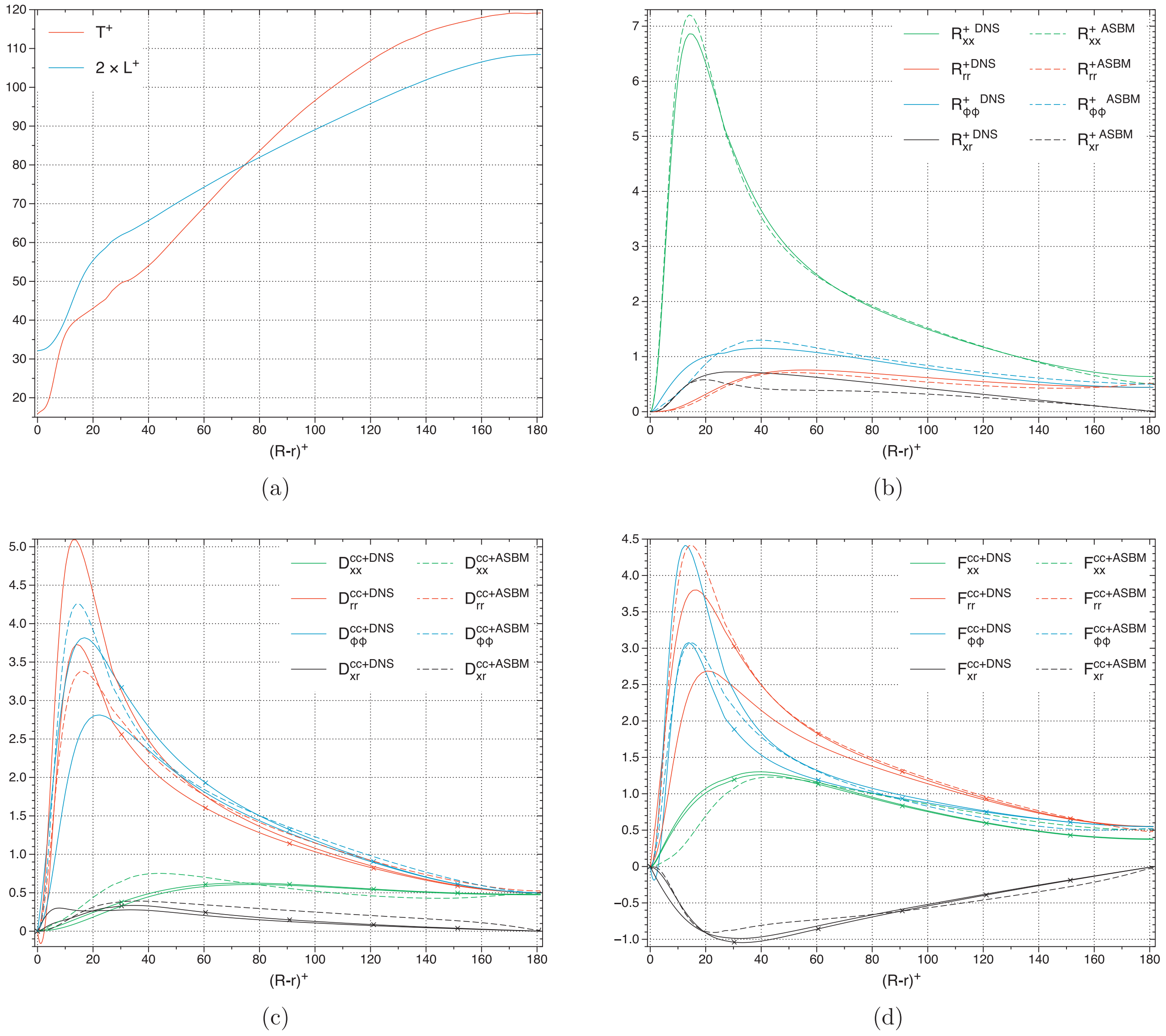

(a) (b) (c) (d)

Fig. B1. Comparison between the ASBM predictions and the DNS data computed via GF and LF. (a) Turbulent time scale and length scale (multiplied by constant factor) as calculated from the DNS simulation. (b) Componentality, (c) Homogenized dimensionality, and (d) Homogenized circulicity tensors. Lines with/without cross symbols represent computation using the LF/GF.

The above values imply

$$u_b = 1.0 \quad \tau_w = 4.683 \times 10^{-3} \quad u_\tau = 6.843 \times 10^{-2} \\ \Rightarrow Re_\tau = 181.34. \tag{A.19}$$

Appendix B. Assessment of the ASBM performance

The Algebraic Structure-Based Model (ASBM) belongs to the family of Structure-Based turbulence Models (SBMs) that incorporate information on the large-scale turbulence structures. The ASBM requires as input the turbulence time and length scales, and the mean flow velocity gradients. Via algebraic relations (that are built to capture turbulent physics) and a differential equation (that incorporates wall effects), the ASBM returns the normalized structure tensors, including the Reynolds stresses. The unnormalized structure tensors are obtained by multiplying with twice the kinetic energy. A full description of the latest version of ASBM is reported in Panagiotou et al. [36].

To demonstrate the ability of ASBM to predict all the components of the structure tensors, we use our DNS data as input to the model. From the DNS data we compute the turbulent kinetic energy k and the pseudo dissipation ϵ (Fig. 16 shows the profiles for these variables). Based on these variables we calculate the turbulent time T and length L scales using the expressions

$$T = \sqrt{\left(\frac{k}{\epsilon}\right)^2 + \left(C_T\sqrt{\frac{\nu}{\epsilon}}\right)^2} \\ L = C_L \max\left(\frac{k^{3/2}}{\epsilon}, C_\eta\left(\frac{\nu^3}{\hat{\epsilon}}\right)^{1/4}\right), \tag{B.1}$$

where $C_T = 6.0$, $C_L = 0.23$, $C_\eta = 70$, $\hat{\epsilon} = \sqrt{\epsilon^2 + \bar{\epsilon}^2}$, and $\bar{\epsilon} = \nu\overline{u_{i,j}}\,\overline{u_{i,j}}$. In Fig. B.1a we report the profiles for these variables. For the turbulent time scale the ASBM uses the above smooth functional relation instead of the classical max operator. For the length scale a similar smooth function is not necessary; in the ASBM the length scale is involved in a differential equation the solution of which is smooth. In the Kolmogorov part of the length scale the mean flow dissipation is included to avoid unreasonably high values when the dissipation decays (i.e. in the corners of a square duct flow configuration). The modification in the Kolmogorov scale was introduced by Reif and Andersson [41]. Non-physical large values of the Kolmogorov scales result in an overgrowth of length scale, which in turn result in an enforced wall blocking [22].

Fig. B.1 compares the ASBM predictions for the structure tensors, and the DNS data computed via the GF and LF. Given the fact that the ASBM was tuned to capture the structure tensors extracted from a DNS of a channel flow (using the LF), its agreement with the respective DNS data in our turbulent pipe flow is not unexpected. The agreement is even higher, especially for the xr components, when the ASBM is coupled with the $k-\epsilon-\overline{v^2}-f$ model [46] which was initially tuned. In this study, we have presented strong arguments in favor of using the GF (instead of LF) for the computation of the structure tensors. This suggests that the ASBM should be retuned to capture the GF results. No attempt was made in the present study to retune the coefficients of the ASBM model. It is interesting to note that the diagonal components of the homogenized tensors D_{ij}^{cc} and F_{ij}^{cc} lack positive semi-definiteness and can in principle attain negative values. This is indeed the case for the DNS data of the LF in the viscous sublayer. On the other hand, it just so happens that the GF data do not have negative values. This is a positive outcome for the ASBM which enforces positive semi-definiteness on the modeled D_{ij}^{cc} and F_{ij}^{cc}.

References

[1] Albets-Chico X, Kassinos S. A consistent velocity approximation for variable–density flow and transport in porous media. J Hydrol 2013;507:33–51.

[2] Apte S, Mahesh K, Moin P, Oefelein J. Large-eddy simulation of swirling particle-laden flows in a coaxial-jet combustor. Int J Multiphase Flow 2003;29(8):1311–31.

[3] Aupoix B, Kassinos S, Langer C. ASBM-BSL: An easy access to the structure based model technology. In: Progress in wall turbulence: understanding and modeling. Springer; 2011. p. 277–85.

[4] Boersma B. A 6th order staggered compact finite difference method for the incompressible Navier-Stokes and scalar transport equations. J Comput Phys 2011;230(12):4940–54.

[5] Boersma B. Direct numerical simulation of turbulent pipe at high Reynolds numbers, velocity statistics and large scale motions. TSFP digital library online. Begel House Inc.; 2013.

[6] Bradshaw P. Inactive motion and pressure fluctuations in turbulent boundary layers. J Fluid Mech 1967;30(02):241–58.

[7] Bradshaw P. The turbulence structure of equilibrium boundary layers. J Fluid Mech 1967;29(04):625–45.

[8] del Álamo J, Jimenez J, Zandonade P, Moser R. Self-similar vortex clusters in the turbulent logarithmic region. J Fluid Mech 2006;561:329–58.

[9] Dubief Y, Delcayre F. On coherent-vortex identification in turbulence. J Turbul 2000;1(1):011.

[10] Eggels J, Unger F, Weiss M, Westerweel J, Adrian R, Friedrich R, Nieuwstadt F. Fully developed turbulent pipe flow: a comparison between direct numerical simulation and experiment. J Fluid Mech 1994;268(1):175–209.

[11] El Khoury G, Schlatter P, Noorani A, Fischer P, Brethouwer G, Johansson A. Direct numerical simulation of turbulent pipe flow at moderately high Reynolds numbers. Flow Turbul Combust. 2013;91(3):475–95.

[12] Fukagata K, Kasagi N. Highly energy-conservative finite difference method for the cylindrical coordinate system. J Comput Phys 2002;181(2):478–98.

[13] Grigoriadis D, Langer C, Kassinos S. Diagnostic properties of structure tensors in turbulent flows. In: Direct and large-Eddy simulation VII. Springer; 2010. p. 41–7.

[14] Ham F, Iaccarino G. Energy conservation in collocated discretization schemes on unstructured meshes. In: Annual research briefs. Center for Turbulence Research, NASA Ames/Stanford University; 2004. p. 3–14.

[15] Ham F, Mattsson K, Iaccarino G. Accurate and stable finite volume operators for unstructured flow solvers. In: Annual research briefs. Center for Turbulence Research, NASA Ames/Stanford University; 2006. p. 243–61.

[16] Jeong J, Hussain F. On the identification of a vortex. J Fluid Mech 1995;285:69–94.

[17] Kassinos S, Akylas E. Advances in particle representation modeling of homogeneous turbulence. From the linear PRM version to the interacting viscoelastic IPRM. In: New approaches in modeling multiphase flows and dispersion in turbulence, fractal methods and synthetic turbulence. Springer; 2012. p. 81–101.

[18] Kassinos S, Reynolds W. A structure-based model for the rapid distortion of homogeneous turbulence. Ph.D. thesis. Thermosciences Division, Department of Mechanical Engineering, Stanford University; 1995.

[19] Kassinos S, Reynolds W. A particle representation model for the deformation of homogeneous turbulence. In: Annual research briefs. Center for Turbulence Research, NASA Ames/Stanford University; 1996. p. 31–50.

[20] Kassinos S, Langer C, Haire S, Reynolds W. Structure-based turbulence modeling for wall-bounded flows. Int J Heat Fluid Flow 2000;21(5):599–605.

[21] Kassinos S, Reynolds W, Rogers M. One-point turbulence structure tensors. J Fluid Mech 2001;428(1):213–48.

[22] Kassinos S, Langer C, Kalitzin G, Iaccarino G. A simplified structure-based model using standard turbulence scale equations: computation of rotating wall-bounded flows. Int J Heat Fluid Flow 2006;27(4):653–60.

[23] Kim H, Kline S, Reynolds W. The production of turbulence near a smooth wall in a turbulent boundary layer. J Fluid Mech 1971;50(1):133–60.

[24] Kim J, Moin P. Application of a fractional-step method to incompressible Navier-Stokes equations. J Comput Phys 1985;59(2):308–23.

[25] Kim J, Moin P, Moser R. Turbulence statistics in fully developed channel flow at low Reynolds number. J Fluid Mech 1987;177(1):133–66.

[26] Kline S, Reynolds W, Schraub F, Runstadler P. The structure of turbulent boundary layers. J Fluid Mech 1967;30(4):741–73.

[27] Langer C, Reynolds W. A new algebraic structure-based turbulence model for rotating wall-bounded flows. Ph.D. thesis. Thermosciences Division, Department of Mechanical Engineering, Stanford University; 2003.

[28] Lee M, Kim J, Moin P. Structure of turbulence at high shear rate. J Fluid Mech 1990;216:561–83.

[29] Loulou P, Moser R, Mansour N, Cantwell B. Direct numerical simulation of incompressible pipe flow using a B-spline spectral method. NASA technical memo 110436; 1997.

[30] Lozano-Durán A, Jiménez J. Time-resolved evolution of coherent structures in turbulent channels: characterization of eddies and cascades. J Fluid Mech 2014;759:432–71.

[31] Lozano-Durán A, Flores O, Jiménez J. The three-dimensional structure of momentum transfer in turbulent channels. J Fluid Mech 2012;694:100–30.

[32] Mahesh K, Constantinescu G, Apte S, Iaccarino G, Ham F, Moin P. Progress toward large-eddy simulation of turbulent reacting and non-reacting flows in complex geometries. In: Annual research briefs. Center for Turbulence Research, NASA Ames/Stanford University; 2002. p. 115–42.

[33] Mahesh K, Constantinescu G, Moin P. A numerical method for large-eddy simulation in complex geometries. J Comput Phys 2004;197(1):215–40.

[34] Moser R, Moin P. Direct numerical simulation of curved turbulent channel flow. NASA technical memo 85974; 1984.

[35] Panagiotou C, Kassinos S. A structure-based model for the transport of passive scalars in homogeneous turbulent flows. Int J Heat Fluid Flow 2016;57:109–29.

[36] Panagiotou C, Kassinos S, Aupoix B. The ASBM-SA turbulence closure: taking advantage of structure-based modeling in current engineering CFD codes. Int J Heat Fluid Flow 2015;52:111–28.

[37] Pinelli A, Uhlmann M, Sekimoto A, Kawahara G. Reynolds number dependence of mean flow structure in square duct turbulence. J Fluid Mech 2010;644:107–22.

[38] Pope S. Turbulent flows. Cambridge University Press; 2000.

[39] Poroseva S, Kassinos S, Langer C, Reynolds W. Structure-based turbulence model: application to a rotating pipe flow. Phys Fluids 2002;14(4):1523–32.

[40] Quartapelle L. Numerical solution of the incompressible Navier-Stokes equations, vol. 113. Birkhäuser Verlag (Basel and Boston); 1993.

[41] Reif B, Andersson H. Prediction of turbulence-generated secondary mean flow in a square duct. Flow Turbul Combust 2002;68(1):41–61.

[42] Reynolds W, Langer C, Kassinos S. Structure and scales in turbulence modeling. Phys Fluids 2002;14(7):2485–92.

[43] Rogers M, Moin P. The structure of the vorticity field in homogeneous turbulent flows. J Fluid Mech 1987;176:33–66.

[44] Satake S, Kunugi T, Himeno R. High Reynolds number computation for turbulent heat transfer in a pipe flow. In: High performance computing. Springer; 2000. p. 514–23.

[45] Smith C, Metzler S. The characteristics of low-speed streaks in the near-wall region of a turbulent boundary layer. J Fluid Mech 1983;129(1):27–54.

[46] Stylianou F, Kassinos S. Computation of the one-point turbulence structure tensors in fully-developed turbulent pipe flow; 2014. WCCM XI - ECCM V - ECFD VI, Barcelona, Spain; URL http://www.wccm-eccm-ecfd2014.org/admin/files/fileabstract/a3450.pdf.

[47] Stylianou F, Kassinos S. The contribution of active and inactive structures to the statistics of a turbulent pipe flow. In: Proceedings of 11th international ERCOFTAC iymposium on engineering turbulence modelling and measurements; 2016.

[48] Stylianou F, Pecnik R, Kassinos S. A general framework for computing the turbulence structure tensors. Comput Fluids 2015;106:54–66.

[49] Townsend A. The structure of turbulent shear flow. 1st ed. Cambridge University Press; 1956.

[50] Townsend A. Equilibrium layers and wall turbulence. J Fluid Mech 1961;11(01):97–120.

[51] Townsend A. The structure of turbulent shear flow. 2nd ed. Cambridge University Press; 1976.

[52] Vartdal M. Computing turbulence structure tensors in plane channel flow. Comput Fluids 2016;136:207–11.

[53] Veenman M. Statistical analysis of turbulent pipe flow: a numerical approach. Ph.D. thesis. Faculty of Mechanical Engineering, Eindhoven University of Technology; 2004.

[54] Vinuesa R, Noorani A, Lozano-Durán A, El Khoury G, Schlatter P, Fischer P, et al. Aspect ratio effects in turbulent duct flows studied through direct numerical simulation. J Turbul 2014;15(10):677–706.

[55] Wagner C, Hüttl T, Friedrich R. Low-Reynolds-number effects derived from direct numerical simulations of turbulent pipe flow. Comput Fluids 2001;30(5):581–90.

[56] Wu X, Moin P. A direct numerical simulation study on the mean velocity characteristics in turbulent pipe flow. J Fluid Mech 2008;608:81–112.

[57] You D, Ham F, Moin P. Discrete conservation principles in large-eddy simulation with application to separation control over an airfoil. Phys Fluids 2008;20(10):101515.